ALMA MATER STUDIORUM
UNIVERSITÀ DI BOLOGNA

Master's Degree in Aerospace Engineering
Space Curriculum

Auto-calibration and alignment methodology validation and characterisation for a STIM300 IMU

SUPERVISOR:
Prof. Marco Sagliano

CANDIDATE:
Beatrice Boccadifuoco

CO-SUPERVISOR:
Prof. Emanuele Di Sotto

15th July 2026
Academic Year 2025/2026

ALMA MATER STUDIORUM
UNIVERSITÀ DI BOLOGNA

Master's Degree in Aerospace Engineering

Space Curriculum

Auto-calibration and alignment methodology validation and characterisation for a STIM300 IMU

SUPERVISOR:
Prof. Marco Sagliano

CANDIDATE:
Beatrice Boccadifuoco

CO-SUPERVISOR:
Prof. Emanuele Di Sotto

15th July 2026

Academic Year 2025/2026

Abstract

This thesis presents the experimental validation of an auto-calibration and auto-alignment methodology for a STIM300 IMU, using a Mitsubishi PA10 robotic arm as a controlled motion platform. The objective is to estimate sensor biases and alignment parameters in a mounted configuration, where the IMU cannot be freely repositioned after integration on its mechanical interface.

The work focuses on accelerometer, inclinometer, and gyroscope biases, together with the misalignment angles between the navigation frame and the IMU frame. Particular attention is given to the coupling between yaw angle and gyroscope bias under static conditions. Since gravity-based measurements allow the estimation of pitch and roll but do not provide heading information, yaw cannot be independently determined from static data alone. For this reason, controlled rotational motion is introduced to provide additional information and separate bias-related effects from yaw-related misalignment effects.

The experimental activity includes a laboratory calibration phase, used to obtain reference bias values and interface-to-IMU misalignment angles, and a real-case procedure, where the IMU is treated as already mounted and only limited static and rotational datasets are used.

The results show that the proposed procedure can estimate the main calibration and alignment quantities from real experimental data. However, yaw estimation and the Y-channel gyroscope bias are highly sensitive to the accuracy of the interface-to-IMU misalignment angles α and β. A sensitivity analysis confirms that small errors in these angles can introduce significant residual contributions when the robot angular velocity is removed from the gyroscope outputs. Finally, a linear same-dataset estimation of α and β is investigated as a possible improvement toward a more autonomous calibration and alignment procedure.

Contents

List of Figures

List of Tables

CHAPTER 1

Introduction

Nowadays, all aerospace systems rely on Guidance, Navigation, and Control (GNC) algorithms to determine their state and execute mission objectives. Within this framework, navigation plays a fundamental role, since it provides the information required to determine the position, velocity, attitude, and angular rates of the system.

Inertial Measurement Units (IMUs) represent one of the core sensors for navigation. They provide measurements of angular rates and specific forces through gyroscopes and accelerometers, respectively. These measurements are integrated over time to estimate the system state, often in combination with external sensors through filtering techniques such as the Kalman Filter [1, 2]. The main IMU error sources considered in this work are introduced in Section 3.2.
However, the integration process makes inertial navigation highly sensitive to sensor errors. In particular, gyroscope bias produces an attitude error that grows linearly with time, while accelerometer bias leads to velocity and position errors that grow linearly and quadratically, respectively. Moreover, attitude errors caused by gyroscope bias affect the projection of the gravity vector into the navigation frame, producing additional acceleration errors that further degrade the navigation solution [1, 2]. As a consequence, even small imperfections in the IMU measurements can lead to significant navigation errors if not properly compensated.
For this reason, the characterization and calibration of IMU error sources represent a critical step in ensuring reliable navigation performance. Among the various error sources, bias and misalignment play a dominant role, as they introduce systematic deviations that directly affect the accuracy of the measured angular rates and specific forces. These deterministic error sources are discussed in Section 3.2.1.

The importance of accurate IMU calibration can be understood by analyzing how sensor errors propagate through the navigation solution.
In inertial navigation, the attitude is obtained by integrating the angular rate measurements provided by the gyroscopes. If a constant bias is present in the angular rate measurement, the estimated attitude error grows linearly with time

$$\delta\theta(t) = b_\omega \cdot t \tag{1.1}$$

where b_ω represents the gyroscope bias.

Similarly, accelerometer measurements are integrated to obtain velocity and position. A constant bias in the acceleration produces a velocity error that grows linearly with time and a position error that grows quadratically

$$\delta v(t) = b_a \cdot t \tag{1.2}$$

$$\delta p(t) = \frac{1}{2}\, b_a \cdot t^2 \tag{1.3}$$

where b_a denotes the accelerometer bias.

Gyroscope bias is particularly critical because it affects not only the attitude estimate, but also the position estimate indirectly. A small error in the attitude leads to an incorrect projection of the gravity vector into the navigation frame. For small angles, the resulting acceleration error can be approximated as

$$\delta a(t) \approx g \cdot \delta\theta(t) \tag{1.4}$$

By substituting Equation 1.1 into Equation 1.4, the acceleration error induced by gyroscope bias becomes proportional to time. This error propagates through integration, leading to a velocity error growing quadratically and a position error growing cubically

$$\delta v(t) \sim \frac{1}{2} g\, b_\omega\, t^2 \tag{1.5}$$

$$\delta p(t) \sim \frac{1}{6} g\, b_\omega\, t^3 \tag{1.6}$$

These relationships show why even small bias values can lead to significant navigation errors if they are not properly estimated and compensated. In practical applications, these effects are often mitigated by combining inertial measurements with external observations through aided navigation techniques [2, 3]. Nevertheless, the performance of these methods strongly depends on the quality of the initial sensor calibration and alignment.

The objective of this thesis is therefore to experimentally validate an auto-calibration and auto-alignment methodology for a STIM300 IMU mounted on a PA10 robotic arm. The work focuses on the estimation of sensor biases and alignment parameters, with particular attention to the coupling between gyroscope bias and yaw-related misalignment under static conditions. To overcome this limitation, controlled rotational motion is exploited to provide additional information and separate bias-induced effects from misalignment effects. The experimental setup is described in Chapter 4, while the laboratory calibration and real-case validation procedures are presented in Chapters 5 and 6, respectively.

CHAPTER 2

State of the Art

The calibration of inertial sensors is traditionally performed using dedicated laboratory equipment and external reference systems, such as optical tracking systems, high-precision turntables, rate tables, or GNSS-based solutions. These approaches allow accurate estimation of sensor parameters, including bias, scale factor, axis non orthogonality, and misalignment terms. In classical strapdown inertial navigation systems, the raw outputs of gyroscopes and accelerometers are corrected through calibration parameters before being integrated to estimate attitude, velocity, and position [1, 2]. For this reason, the characterization of inertial sensor errors is considered a fundamental preliminary step in the design and operation of inertial navigation systems.

Traditional calibration procedures are generally based on the comparison between the IMU outputs and known reference quantities. This allows the identification of deterministic sensor parameters under controlled conditions [4, 5]. These methods can provide high accuracy, especially when the reference equipment is significantly more accurate than the sensor under test. However, such calibration procedures are often costly, time-consuming, and require specialized infrastructure. Moreover, they are typically performed offline, so they do not account for variations in sensor behavior across different operational conditions or for installation-dependent effects after the IMU has been mounted on its final platform.

This limitation is particularly relevant for MEMS-based IMUs, which are widely used because of their compact size, low mass, reduced power consumption, and ease of integration. However, compared with higher-grade inertial sensors, MEMS devices are generally more affected by bias variations, thermal sensitivity, scale-factor errors, and mounting imperfections.
For MEMS inertial sensors, several calibration strategies have been proposed

in the literature to reduce the dependence on laboratory equipment and to make the calibration process more practical for low-cost and field-deployable systems.

Among these strategies, multi-position calibration methods represent an important class of approaches. In these procedures, the IMU is placed in several different static orientations and the calibration parameters are estimated by exploiting the consistency of the measured gravity vector. Syed et al. proposed a multi-position calibration method for MEMS inertial navigation systems, showing that deterministic parameters can be estimated without requiring special aligned mounting, although a rotation-rate reference is still used for the gyroscope calibration [4]. This type of method is useful because the calibration does not require perfectly known sensor orientations, provided that the IMU is placed in sufficiently different static attitudes.

Other works have focused on calibration procedures that are even easier to implement and do not require external calibration equipment. Tedaldi et al., for example, proposed a method based on hand motion and automatic detection of static intervals, allowing the estimation of scale factors, misalignment parameters, and biases for low-cost IMUs [5]. These approaches are attractive because they reduce the cost and complexity of the calibration process. Nevertheless, their applicability depends on the possibility of moving the sensor through a sufficiently large set of orientations. When the IMU is already mounted on a launcher, vehicle, robotic arm, or mechanical interface, such free repositioning may not be possible.
The use of static intervals in these approaches is relevant for the bench characterization performed in this work (see Section 5.2), since both methods exploit static intervals and the gravity vector to obtain reference information on the accelerometer measurements. However, the objective here is not to perform a complete multi-parameter IMU calibration, but to obtain reference bias values to support the validation of the proposed auto-calibration and auto-alignment procedure.

More generally, stochastic and time-varying error contributions in inertial sensors are commonly characterized using Allan variance analysis. This technique allows the identification of different random error terms by analyzing how the measurement variance changes with the averaging time. It is widely used to characterize inertial sensor noise, bias instability, and random walk contributions [6, 7]. In this dissertation, these effects are acknowledged as relevant limitations. However, the proposed calibration procedure focuses on deterministic quantities, namely sensor biases and alignment parameters, which are assumed to remain approximately constant over the duration of the experiment.

In particular, a fundamental characteristic of inertial sensors is that the bias is not uniquely defined in different operating conditions. The initial bias value may vary significantly between different power cycles of the sensor. This phenomenon, commonly referred to as turn-on bias variation, represents one of the main sources of uncertainty in practical applications. It arises from internal sensor conditions, such as temperature distribution, electronic initialization, and other effects that are not perfectly repeatable between successive activations. As a result, the bias cannot be reliably predicted a priori from a previous calibration and should be estimated at each sensor start-up when high accuracy is required.
The turn-on bias variation is particularly critical in applications where high accuracy is required from the early stages of operation. In such cases, an initial on-site calibration phase is necessary to estimate the current bias before mission execution. However, the need for on-site calibration is not only related to turn-on bias variation, but also to the fact that the alignment between the IMU and the reference frame depends on the actual mounting configuration. A calibration performed before integration may accurately characterize the sensor as a standalone unit, but it does not necessarily describe the final orientation of the IMU with respect to the navigation frame or to the mechanical interface on which it is installed.

Currently, to achieve the required accuracy on-site and compensate for the limitations of inertial-only initialization, several external aids are commonly employed in calibration, alignment, and aided navigation procedures [2, 3]. These include:

- **GNSS Integration:** Used to provide absolute velocity and position references, which help bound the drift caused by uncalibrated biases;
- **Magnetometers:** Often used as an external heading reference to aid the unobservable yaw angle, though they are highly susceptible to local magnetic disturbances;
- **Optical Tracking or Star Trackers:** In aerospace applications, these systems provide precise attitude references but increase system complexity, weight, and cost;
- **High-Precision Mechanical Benchmarks:** On-site calibration may require the IMU to be manually or mechanically aligned with surveyed external landmarks, optical prisms, or mechanical references.

Examples of such external references and calibration supports are also discussed in practical IMU calibration literature, where mechanical platforms, optical tracking systems, and GPS-based measurements are considered as possible aids for estimating sensor errors and alignment parameters [5].
GNSS/INS integration is widely used to limit the long-term drift of inertial navigation, while other sensors such as magnetometers, cameras, optical tracking systems, or star trackers can provide additional heading or attitude information depending on the operational environment [2, 3].

However, while effective, these external supports introduce significant operational constraints and costs. A trade-off remains between calibration accuracy, required infrastructure, and level of autonomy. In particular, methods that achieve full parameter observability often rely on external references or specialized hardware. This motivates the development of calibration procedures capable of operating with minimal external support, while still ensuring sufficiently accurate sensor characterization.
From a market and operational perspective, a system that requires no external aiding is highly desirable: it simplifies the initialization process and allows greater autonomy in environments where GNSS, optical signals, or magnetic references are unavailable or unreliable. This aspect is especially relevant for applications in which the IMU is already mounted on the final platform and cannot be freely repositioned after integration.

A key challenge in IMU calibration arises from the coupling between sensor bias and misalignment effects. In static conditions, the measurement model exhibits an observability limitation, in which certain parameters cannot be independently identified [8]. This limitation is not only related to the choice of the estimation algorithm, but to the information content of the measurements themselves. If two unknown quantities produce equivalent effects on the measured outputs under a given experimental condition, no estimator can separate them without additional information or excitation.
This limitation makes it difficult to distinguish between bias-induced errors and misalignment effects, as both contribute to the measured signals in a similar manner. As a result, traditional static calibration approaches are not sufficient to fully characterize the system. For instance, a common approach consists in keeping the sensor at rest for a short period after power-up. Under static conditions, gravity measurements allow the estimation of the leveling angles, while gyroscope bias can be partially estimated by averaging the angular rate measurements over time. However, due to the lack of excitation, the yaw angle remains unavailable without an external reference or sufficiently informative motion, and a coupling between yaw and gyroscope bias prevents

their independent estimation (see Chapter 6).

This observability issue has been investigated in the strapdown INS alignment literature. Wu et al. analyzed the observability of strapdown INS alignment from a global perspective, showing that attitude maneuvers can improve the estimability of alignment states and inertial sensor biases [8]. Their work highlights that motion can provide information that is not available in purely static conditions. This is important for the following thesis, because it supports the idea that the solution to the bias-alignment coupling problem is not only algorithmic, but also related to the type of excitation imposed on the IMU.
Indeed, to overcome this issue, a method utilizing a rotating platform is proposed. By introducing controlled rotational motion, the system is dynamically excited [8, 9, 10]. In this configuration, while the bias remains approximately constant over the duration of the experiment, the misalignment effect varies as a function of the rotation angle ψ. This physical variation allows the algorithm to decouple the two phenomena, enabling the simultaneous estimation of both bias and alignment parameters without any external measurement aiding (see Chapter 6).

Rotation-based calibration and alignment methods have been studied in different forms in the literature. In rotation modulation techniques, the IMU is deliberately rotated so that alignment sensor errors are transformed into periodic or varying components. Depending on the adopted rotation scheme, this can help separate, average, or estimate error terms that would otherwise remain coupled in static conditions.
Du et al. showed that rotary motions can improve the observability of a MEMS-based inertial system [9]. Their results also show that rotation improves the estimability of several error states, although heading-related quantities may remain more difficult to observe depending on the rotation scheme and available measurements.
Xing et al. proposed a MEMS IMU self-alignment method based on rotation modulation, confirming the interest of controlled rotation for reducing the effect of inertial sensor errors during alignment [10].

Consequently, in this context, the development of an autonomous calibration and alignment method represents a significant advantage. The approach considered in this thesis is positioned between classical laboratory calibration and fully aided navigation methods. Laboratory calibration provides accurate reference values, but requires dedicated infrastructure and may not represent the current turn-on condition or final mounted configuration of the IMU (see chapter 5). Aided methods improve observability, but rely on additional sensors or external references. Static initialization is simple, but cannot fully resolve yaw-related ambiguities. Controlled rotation offers a practical compromise, since it introduces additional information through motion while preserving a relatively simple and autonomous experimental setup (see Chapter 6).

2.1 Motivation and Interests

The objective of this work is to investigate and experimentally validate a calibration approach based on controlled rotational motion, enabling the simultaneous estimation of sensor bias and alignment parameters without external aiding. This approach aims to overcome the limitations of static calibration and to provide a practical solution for autonomous IMU initialization.
As mentioned above, the comprehensive characterization of an IMU cannot be achieved under static conditions. This limitation is primarily due to a coupling effect between the gyro bias and the yaw angle in static equations (see Equation 6.24). To overcome this, a method utilizing a rotating platform is proposed, enabling both auto-calibration and auto-alignment of the IMU, as described in Chapter 6.

This procedure, tested experimentally, confirms that when the IMU is mounted on a rotating platform, it is possible to:

- Estimate the systematic sensor biases;
- Compute the Euler angles describing the misalignment (yaw, pitch, roll) between the IMU and the navigation frames;
- Decouple the effects of misalignment from those caused by biases.

Generally, an Inertial Measurement Unit is characterized by several errors. The most important intrinsic error on the timescale of interest is bias. Nevertheless, the IMU output data are also affected by another type of error that is related to the angles formed between the navigation frame and the IMU one: $[\psi, \theta, \phi]$. In fact, even if the IMU should ideally be aligned with $[\hat{\boldsymbol{N}}, \hat{\boldsymbol{W}}, \hat{\boldsymbol{U}}]$ directions, perfect alignment is never achieved in practice. Hence, small angles of misalignment are always present and their effect introduces constant offsets in the measured accelerations and angular rates, which represent the projections of the sensed vectors along the IMU frame axes (see Figure 3.8). As a consequence, despite their different physical nature, systematic biases and misalignment effects appear intertwined in the raw IMU output data.

The objective of the following study is to extract the bias values and to separate their effects from those caused by the angles of misalignment.

The complete methodology and its experimental validation are presented in Chapters 5, 6 and 7.

CHAPTER 3

Theoretical Background

This chapter introduces, in Section 3.1, the reference frames used throughout the thesis and defines the rotation matrices adopted to describe the relative orientation between them.
In addition, Section 3.2 summarizes the main IMU error sources considered in the calibration and alignment procedure.

3.1 Reference Frames and Rotation Matrices

The reference frames considered in this work are defined in this section. They are required to describe the orientation of the IMU with respect to the navigation frame, the robotic arm, and the mechanical interface on which the sensor is mounted. The frame definition adopted in this thesis follows the internal methodology proposed in [11, 12], which also provides the mathematical procedure experimentally validated in this work.

Inertial Frame (Earth-Centered Inertial – ECI)

The ECI frame is centered at the Earth's center of mass. Its axes are denoted by $[\hat{X}_i, \hat{Y}_i, \hat{Z}_i]$, as shown in Figure 3.1.
In this work, it is introduced to define the Earth rotation vector $\boldsymbol{\Omega}_E$.

- $\hat{\boldsymbol{Z}}_i$ is aligned with the Earth rotation vector $\boldsymbol{\Omega}_E$;
- $\hat{\boldsymbol{X}}_i$ and $\hat{\boldsymbol{Y}}_i$ lie in the equatorial plane.

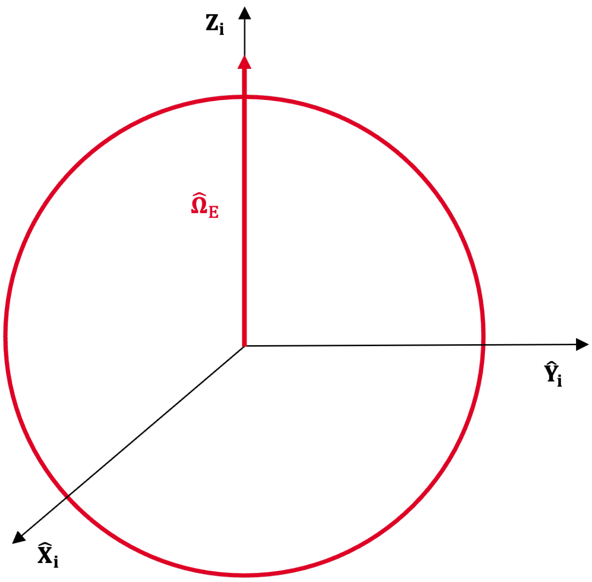

FIGURE 3.1: Definition of the Earth-Centered Inertial (ECI) frame [$\hat{\boldsymbol{X}}_i$, $\hat{\boldsymbol{Y}}_i$, $\hat{\boldsymbol{Z}}_i$]. The Earth rotation vector $\boldsymbol{\Omega}_E$ has been represented in this frame.

Navigation Frame - (NAV)

The navigation frame is a local topocentric frame fixed to the experimental site. Its origin is located at the point where the IMU is assumed to operate, defined by the latitude λ and longitude Φ.
The frame axes are denoted by $[\hat{\boldsymbol{N}}, \hat{\boldsymbol{W}}, \hat{\boldsymbol{U}}]$, as shown in Figures 3.2 and 3.3. The axes are defined as follows:

- the X-axis is aligned with the North direction ($\hat{\boldsymbol{N}}$);
- the Y-axis is aligned with the West direction ($\hat{\boldsymbol{W}}$);
- the Z-axis is aligned with the Up direction ($\hat{\boldsymbol{U}}$).

Therefore, the navigation frame adopted in this thesis follows a North-West-Up convention.

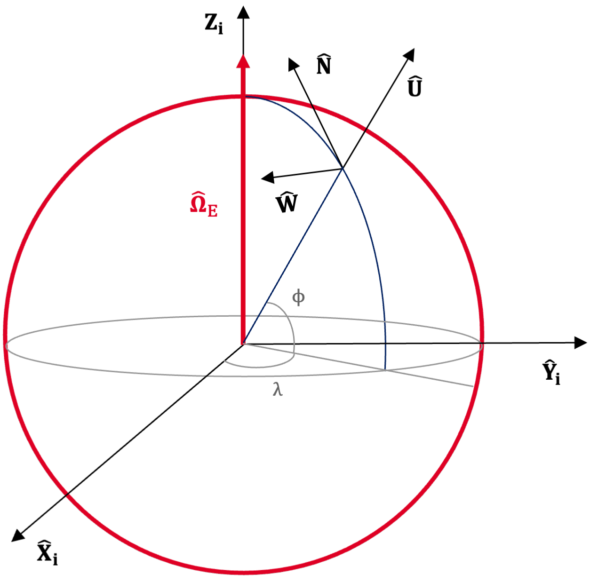

FIGURE 3.2: Definition of the navigation (NAV) frame [$\hat{\boldsymbol{N}}$, $\hat{\boldsymbol{W}}$, $\hat{\boldsymbol{U}}$]. The angles λ and Φ represent respectively the latitude and the longitude of the launch site.

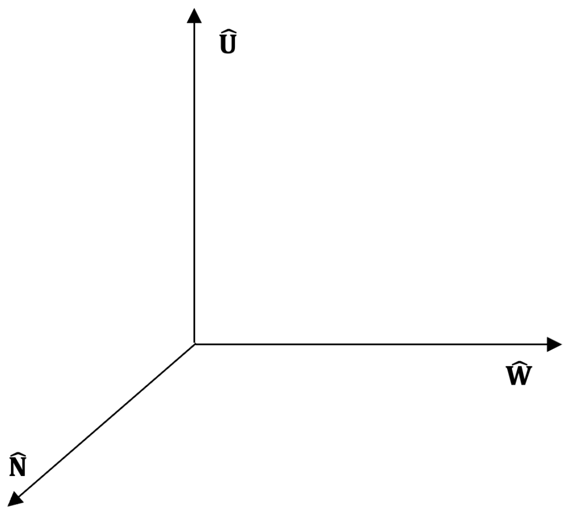

FIGURE 3.3: Definition of the positive directions of the navigation frame [$\hat{\boldsymbol{N}}$, $\hat{\boldsymbol{W}}$, $\hat{\boldsymbol{U}}$]

Robot frame - (Rob)

The robot frame is attached to the base of the PA10 robotic arm, which is used to move the IMU to perform the experiments and collect data.

The reference frame is used to describe the motion imposed by the robotic arm during the experimental campaign and to define the orientation of the mechanical interface supporting the IMU.
The technical characteristics of the PA10 robotic arm and of the STIM300 IMU are described in Section 4.1, and the PA10 is shown in Figure 3.4.

Ideally, the robot frame should be aligned with the navigation frame. In practice, a small misalignment may exist between the robot base and the navigation frame. However, this contribution is assumed to be negligible in the present analysis, so the robot frame is considered aligned with the navigation frame.

FIGURE 3.4: Picture of the PA10 robotic arm.

Interface Frame - (int)

The interface frame is attached to the interface which the IMU is mounted on. Ideally, this frame should be aligned with the robot frame and, consequently, with the navigation frame. However, due to manufacturing tolerances, 3D-printing inaccuracies, and mounting imperfections, a non-negligible misalignment exists between the interface frame and the navigation frame.

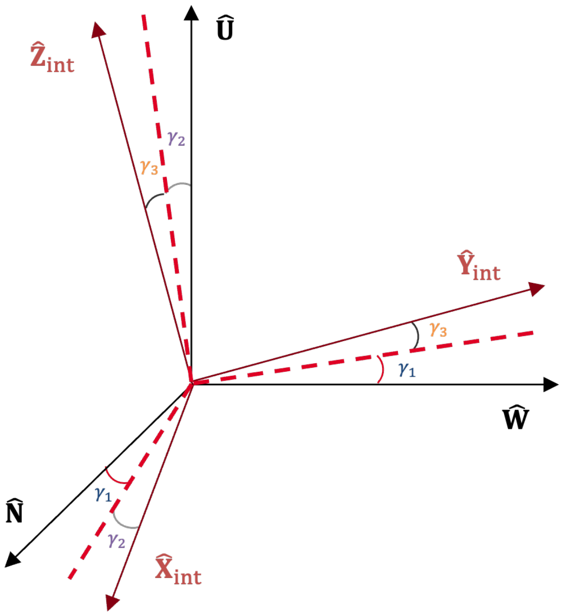

FIGURE 3.5: Representation of the 3-2-1 Euler rotations from the navigation frame [$\hat{\boldsymbol{N}}$, $\hat{\boldsymbol{W}}$, $\hat{\boldsymbol{U}}$] to the interface frame [$\hat{\boldsymbol{X}}_{int}$, $\hat{\boldsymbol{Y}}_{int}$, $\hat{\boldsymbol{Z}}_{int}$]. The angles [$\gamma_1$, γ_2, γ_3] are defined.

This misalignment is described by the Euler angles $[\gamma_1, \gamma_2, \gamma_3]$ and by the corresponding rotation matrix R^{int}_{NAV}, defined according to a 3-2-1 rotation sequence.

The adopted convention is represented in Figure 3.5, while the explicit expression of R^{int}_{NAV} is reported in Section 6.1, where the interface-to-navigation rotation is used in the inclinometer bias estimation procedure (see Equation 6.3).

IMU Frame - (IMU)

The IMU frame is defined by the sensing axes of the STIM300 IMU and is denoted by [$\hat{\boldsymbol{X}}_{IMU}$, $\hat{\boldsymbol{Y}}_{IMU}$, $\hat{\boldsymbol{Z}}_{IMU}$], as shown in Figure 3.6.

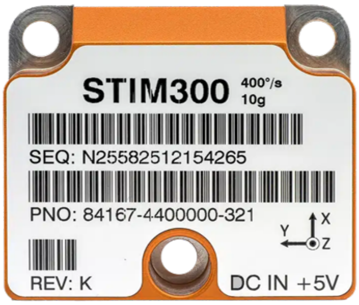

FIGURE 3.6: IMU Figure showing the direction of the IMU frame axes: $[\hat{\boldsymbol{X}}_{IMU}, \hat{\boldsymbol{Y}}_{IMU}, \hat{\boldsymbol{Z}}_{IMU}]$

The IMU frame is misaligned with respect to:

- The navigation frame - due to mounting and orientation;
- The interface frame - due to mechanical inaccuracies.

Two relative orientations are therefore considered:

- The orientation of the IMU frame with respect to the interface frame, described by the rotation matrix R_{int}^{IMU} and by the angles $[\alpha, \beta, 0]$, as shown in Figure 3.7 and in Equation 6.1;

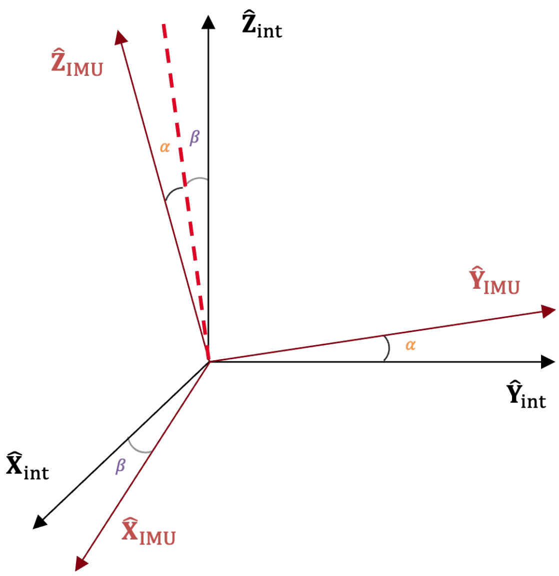

FIGURE 3.7: Representation of the 3-2-1 Euler rotations from the interface frame $[\hat{\boldsymbol{X}}_{int}, \hat{\boldsymbol{Y}}_{int}, \hat{\boldsymbol{Z}}_{int}]$ to the IMU frame $[\hat{\boldsymbol{X}}_{IMU}, \hat{\boldsymbol{Y}}_{IMU}, \hat{\boldsymbol{Z}}_{IMU}]$. The angles $[\alpha, \beta, 0]$ are defined.

- The orientation of the IMU frame with respect to the navigation frame, described by the rotation matrix R_{NAV}^{IMU} and by the yaw, pitch, and roll angles $[\psi, \theta, \phi]$, as shown in Figure 3.8 and in Equation 3.2.

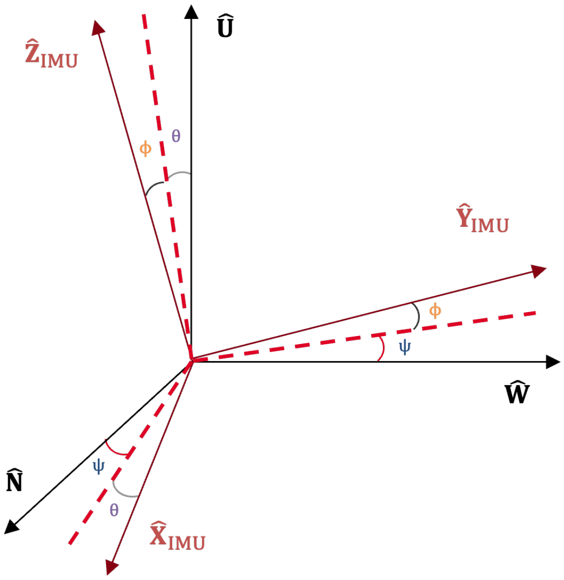

FIGURE 3.8: Representation of the 3-2-1 Euler rotations from the navigation frame $[\hat{\boldsymbol{N}}, \hat{\boldsymbol{W}}, \hat{\boldsymbol{U}}]$ to the IMU frame $[\hat{\boldsymbol{X}}_{IMU}, \hat{\boldsymbol{Y}}_{IMU}, \hat{\boldsymbol{Z}}_{IMU}]$. The angles $[\psi, \theta, \phi]$ are defined.

The total rotation from the navigation frame to the IMU frame is obtained by composing the rotation from the navigation frame to the interface frame and the rotation from the interface frame to the IMU frame

$$R_{NAV}^{IMU} = R_{int}^{IMU} \cdot R_{NAV}^{int}$$

To understand how the 3-2-1 consecutive rotations work, it can be taken, as an example, the composition of rotations for the $[\psi, \theta, \phi]$ set of angles.
The single rotation matrices around the 3rd, the 2nd and the 1st axes of the NAV frame are:

$$R_3(\psi) = \begin{bmatrix} \cos(\psi) & \sin(\psi) & 0 \\ -\sin(\psi) & \cos(\psi) & 0 \\ 0 & 0 & 1 \end{bmatrix} \tag{3.1a}$$

$$R_2(\theta) = \begin{bmatrix} \cos(\theta) & 0 & -\sin(\theta) \\ 0 & 1 & 0 \\ \sin(\theta) & 0 & \cos(\theta) \end{bmatrix} \tag{3.1b}$$

$$R_1(\phi) = \begin{bmatrix} 1 & 0 & 0 \\ 0 & \cos(\phi) & \sin(\phi) \\ 0 & -\sin(\phi) & \cos(\phi) \end{bmatrix} \tag{3.1c}$$

Therefore, the rotation matrix from the navigation frame to the IMU frame is obtained as

$$R_{NAV}^{IMU} = R_1(\phi) \cdot R_2(\theta) \cdot R_3(\psi)$$

Indeed, as stated before, a 3-2-1 scheme rotation is used.
Hence, the full matrix can be computed by carrying out the matrix product:

$$R_{NAV}^{IMU} = \begin{bmatrix} \cos(\theta)\cos(\psi) & \cos(\theta)\sin(\psi) & -\sin(\theta) \\ -\cos(\phi)\sin(\psi)+\sin(\phi)\sin(\theta)\cos(\psi) & \cos(\phi)\cos(\psi)+\sin(\phi)\sin(\theta)\sin(\psi) & \sin(\phi)\cos(\theta) \\ \sin(\phi)\sin(\psi)+\cos(\phi)\sin(\theta)\cos(\psi) & -\sin(\phi)\cos(\psi)+\cos(\phi)\sin(\theta)\sin(\psi) & \cos(\phi)\cos(\theta) \end{bmatrix} \tag{3.2}$$

The same 3-2-1 convention is adopted for the other rotation matrices used in this thesis, with the corresponding Euler angles associated with each pair of reference frames.

3.2 IMU Model & Error Sources

Inertial Measurement Units are affected by multiple error sources that limit the accuracy of the measured angular rates and specific forces. These errors can be classified into deterministic and stochastic, depending on whether they can be modeled as finite parameters or as random processes. [1, 2].

Deterministic errors include bias, scale factor, and misalignment between the IMU and the navigation reference frames. These components can, in principle, be estimated and compensated through calibration procedures. On the other hand, stochastic errors arise from sensor noise and time-varying effects, and are typically characterized using statistical methods, such as Allan variance analysis [6, 7].

3.2.1 Deterministic Errors

Bias

Bias is a constant offset that affects the sensor output. In gyroscopes, it introduces an error in the measured angular rate, which, when integrated over time, leads to a linearly growing error, as shown in Equation 1.1.

In this work, the bias is modeled as constant over the duration of each experiment and is estimated through dedicated calibration procedures. This assumption is justified by the limited duration of the experimental tests, during which long-term bias variations are assumed to be negligible. However, the bias value may vary between different sensor activations due to turn-on bias variation, as discussed in Chapter 2. This motivates the need for an on-site calibration procedure, rather than relying only on previously calibrated laboratory values.

Bias Drift

Although the bias can be approximated as constant over short time intervals, it may exhibit slow variations when observed over longer time scales. This behavior is commonly referred to as bias drift or bias instability.
Unlike fixed bias, bias drift cannot be modeled as a deterministic parameter, as it is influenced by complex and partially unpredictable factors such as temperature fluctuations, electronic noise, and internal sensor dynamics. For this reason, its characterization typically requires statistical tools, such as Allan variance analysis.
Bias instability is often associated with low-frequency noise components, such as pink noise (1/f noise), which dominates at intermediate time scales and defines a lower bound on the achievable sensor accuracy. [6, 7].

These time-varying effects limit the validity of any calibration performed at a single time instant, as the estimated bias may change during operation. Consequently, bias drift cannot be fully compensated through a one-time calibration procedure and typically requires continuous estimation techniques, such as filtering methods (like Kalman Filter).

In this work, bias drift is not explicitly modeled, as the experiments are conducted over time intervals in which bias variations can be reasonably assumed to be negligible. However, its presence is acknowledged as a fundamental limitation affecting the long-term accuracy of the estimation process.

Scale Factor Error

Scale factor error represents a proportionality mismatch between the true physical input and the measured output. This error causes the sensor to either overestimate or underestimate the magnitude of the measured quantity.

While scale factor errors can be significant in high-dynamics applications, their effect is less critical in quasi-static conditions, where the magnitude of the measured signals is limited. For this reason, scale factor calibration is not the primary focus of this study, which centers on pre-launch calibration.

Misalignment

Misalignment refers to the angular discrepancy between the sensor (IMU) axes and the reference (navigation) frame. Even small misalignment angles cause the measured quantities to be projected onto incorrect axes, introducing systematic errors in both angular rate and acceleration measurements. The relative orientation between the navigation frame and the IMU frame is described by the Euler angles $[\psi, \theta, \phi]$, as shown in Figure 3.8.

In the present work, misalignment is one of the main quantities to be estimated. Its effect is particularly relevant because, under static or poorly excited conditions, misalignment contributions can appear in the sensor outputs in a way that is difficult to distinguish from bias. This coupling between bias and misalignment represents one of the central challenges addressed by the proposed calibration and alignment procedure.

3.2.2 Random Errors

White Noise

In addition to deterministic error sources, IMU measurements are affected by stochastic noise, which is commonly modeled as white noise with zero mean.

In this work, the influence of white noise is mitigated by averaging the sensor measurements over a sufficiently long time interval. Since white noise has zero mean, its contribution decreases as the averaging time increases, allowing the underlying deterministic components to be more clearly identified.
This approach relies on the assumption that the deterministic components remain approximately constant over the observation interval, while the stochastic noise averages out. However, averaging does not eliminate noise completely, it only reduces its effect. The averaging interval must therefore be chosen as a compromise, it should be long enough to reduce random noise, but short enough for time-varying effects, such as bias drift, to remain negligible.

Angular Random Walk

When white noise in the gyroscope output is integrated over time, it produces a random error, proportional to the square root of time, in the estimated angle. This phenomenon is known as angular random walk. Unlike bias, which produces a deterministic drift, angular random walk introduces a random dispersion in the estimated attitude.

Stochastic error processes in inertial sensors are commonly characterized using Allan variance analysis. By studying how the measurement variance changes with the averaging time, Allan variance allows different noise components to be identified, including white noise, angular random walk, and bias instability [6, 7]. This information is useful to determine the dominant error sources over different time scales and to determine which effects can be neglected within the duration of the experiment.

Based on these considerations, this work focuses on the estimation and calibration of deterministic error components, specifically bias and misalignment between the IMU and navigation frames.
Other error sources, such as scale factor error, angular random walk, and bias drift, are not explicitly estimated, as they require different modeling and identification approaches. Their presence is nevertheless acknowledged as a limiting factor in the achievable estimation accuracy, as discussed in Chapters 7 and 8.

CHAPTER 4

Experimental Set Up – Data Collection

4.1 STIM300 IMU and PA10 Robotic Arm: Specifics and Characteristics

The experimental activity was carried out using a STIM300 IMU mounted on a Mitsubishi PA10 robotic arm, as shown in Figure 4.1. This setup was selected to provide controlled static orientations and repeatable rotational motion for the validation of the auto-calibration and auto-alignment procedure.
The STIM300 is a MEMS-based inertial measurement unit designed for high-accuracy motion sensing and stabilization applications. It integrates three orthogonal gyroscopes, three accelerometers, and three inclinometers within a compact thermally calibrated unit [13, 14].

The gyroscopes provide angular rate measurements with a full-scale range of $\pm 400\,{}^{\circ}\!/_{s}$, a bias instability of the order of $0.3\,{}^{\circ}\!/_{h}$, and an angular random walk of approximately $0.15\,{}^{\circ}\!/_{\sqrt{h}}$. Despite the high performance of the sensor, a dedicated calibration procedure is still required when accurate initialization is needed, because the current bias value may differ from previously calibrated values due to turn-on bias variation, as discussed in Chapter 2 and Section 3.2.1.

The accelerometers measure specific force with a range of ± 10 g and exhibit a bias instability of approximately 0.04 mg [13]. Under static or quasi-static conditions, accelerometer measurements provide information about the local gravity direction and can therefore be used to estimate the roll ϕ and pitch θ angles. However, since gravity does not provide heading information, accelerometers alone cannot be used to determine the yaw angle ψ.

In addition to accelerometers, the STIM300 includes dedicated inclinometers. These sensors are designed to measure low-frequency acceleration components associated with gravity and provide stable inclination information under quasi-static conditions. Compared with accelerometers, inclinometers offer improved stability for inclination estimation, at the cost of reduced bandwidth [13]. For this reason, they are particularly useful for the estimation of roll and pitch angles in the calibration procedure.
Although the inclinometer bandwidth is reduced, in the calibration procedure developed in this work, inclinometer biases are explicitly estimated and removed from the static inclinometer measurements before computing the pitch θ and roll ϕ angles. This correction is introduced because even small offsets in the inclinometer outputs can affect the attitude angles derived from gravity measurements and, consequently, the accelerometer bias estimation.
The estimation of the inclinometer biases is described in Section 6.1, while their use in the computation of pitch, roll, and accelerometer biases is presented in Section 6.2.

FIGURE 4.1: Picture of the IMU mounted on the PA10 robotic arm in the laboratory.

Both accelerometers and inclinometers rely on the observation of the gravity vector. Therefore, they provide information about pitch and roll, but not about yaw. As a consequence, the yaw angle remains unobservable in the absence of external references or dynamic excitation.

This limitation leads to a coupling between yaw and gyroscope bias under static conditions, which prevents their independent estimation, as shown in Equation 6.24. The resolution of this coupling represents one of the main challenges addressed in this work.

The STIM300 is therefore used as the primary sensing unit for bias estimation and alignment analysis. The combination of gyroscopes, accelerometers, and inclinometers provides a rich measurement set, while still exhibiting the fundamental observability limitations that motivate the use of controlled rotation for calibration purposes.
Moreover, it is also important to express the vectors sensed by the IMU.
The vectors sensed by the IMU are expressed with respect to the navigation frame defined in Section 3.1.
Under static conditions, the accelerometers and inclinometers measure the specific force associated with the reaction to gravity, indicated as $\mathbf{f}_0$. In the navigation frame, this vector is written as

$$\mathbf{f}_0 = g_0 \cdot \hat{\boldsymbol{U}} \tag{4.1}$$

where g_0 is the local gravity magnitude and $\hat{\boldsymbol{U}}$ is the Up direction of the navigation frame, as shown in Figure 4.2.

The Earth rotation vector, indicated as $\boldsymbol{\Omega}_E$, is also expressed in the navigation frame as

$$\boldsymbol{\Omega}_E = \Omega_E \cos(\lambda) \cdot \hat{\boldsymbol{N}} + \Omega_E \sin(\lambda) \cdot \hat{\boldsymbol{U}} \tag{4.2}$$

where λ is the latitude of the experimental site. This vector is represented in Figure 4.3.

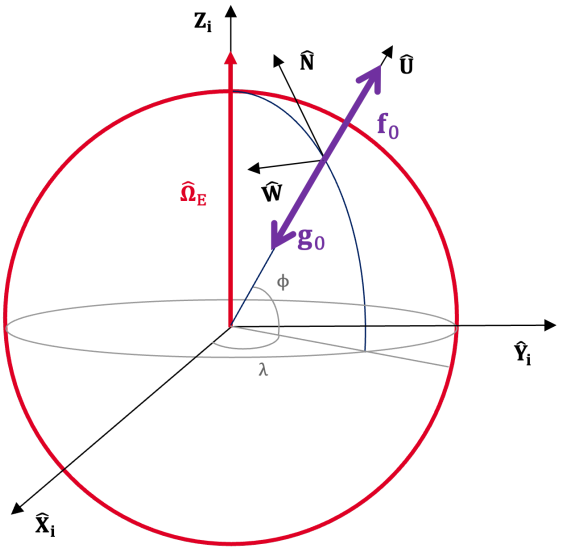

FIGURE 4.2: Definition of the gravity reaction force $\mathbf{f}_0$ and the gravity force $\mathbf{g}_0$ in the navigation frame.

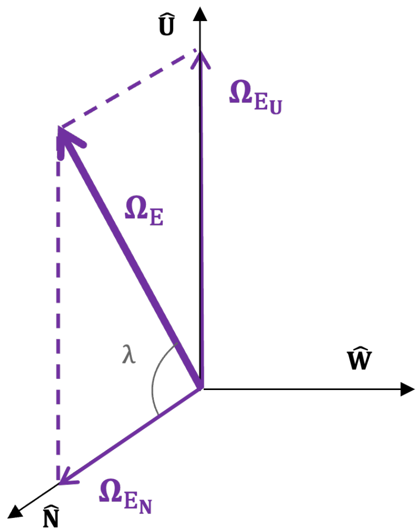

FIGURE 4.3: Definition of $\mathbf{\Omega}_E$ in the navigation frame.

In addition to the IMU, the experimental setup includes the Mitsubishi PA10 robotic arm. The PA10 is a general-purpose robotic manipulator whose control architecture includes base, and tool coordinate systems [15]. The PA10 robotic arm is shown in Figure 4.4.

The PA10 is a seven degrees-of-freedom (7-DoF) robot, providing kinematic redundancy that is particularly advantageous for tasks requiring precise orientation control, such as controlled rotation of an onboard sensor. The robot is actuated by AC servomotors and equipped with position sensors, enabling accurate joint control, making it suitable for fine manipulation and calibration tasks [15].
An important feature of the PA10 is its open architecture, which allows direct access to low-level control and facilitates the integration of external sensors and custom control algorithms. This makes the platform particularly suitable for experimental validation and calibration procedures. Indeed, thanks to this feature, it was possible to perform different experiments by controlling the robot through a set of quaternions [15].

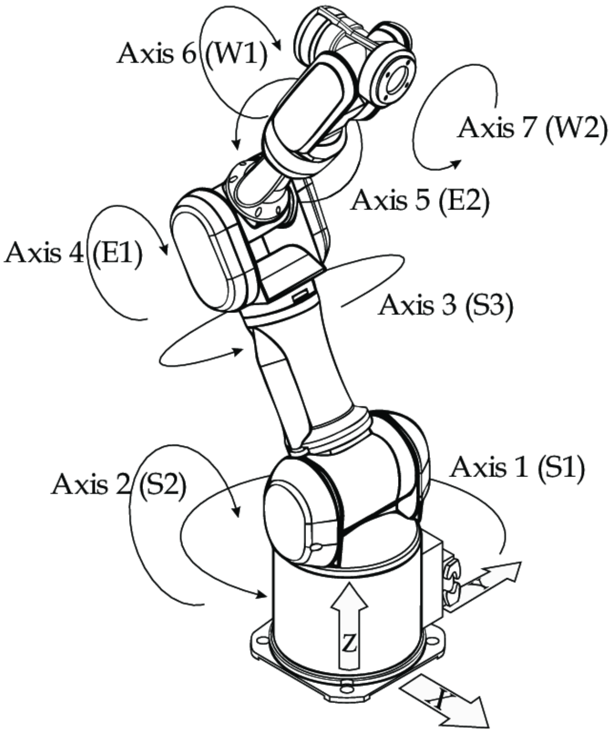

Figure 4.4: PA10 7-DoF.

The use of the PA10 robotic arm is essential for two reasons. First, it allows the collection of static data in controlled configurations, which are used to estimate the bench true bias values in Section 5.2. Second, it provides controlled rotational excitation, which is required to overcome the observability limitations of purely static conditions and to separate bias-induced effects from misalignment-induced effects in the real-case procedure described in Chapter 6.

4.2 Experiment Schedule: Data Collection Protocol

The experimental campaign carried out with the PA10 robotic arm is divided into two main parts.

The first one is designed to obtain reference quantities for the validation of the proposed method. In particular, it is used to compute the bench true bias

values and the interface-to-IMU misalignment angles α and β.
These quantities are later assumed as reference values in the real-case validation procedure.
The bench true bias estimation is described in Section 5.2, while the computation of α and β is presented in Section 5.3.

The second part of the experimental campaign is designed to reproduce a real-case scenario. In this phase, specific static and rotational datasets are collected to validate the auto-calibration and auto-alignment procedure described in Chapter 6. The objective is to simulate the calibration process as if the sensor were installed on a launcher, where free repositioning of the IMU is not possible.

FIGURE 4.5: Picture of the IMU mounted on the PA10 robotic arm during the experiment performed to evaluate the bench true biases.

Before introducing the mathematical formulation and the data analysis, it is useful to summarize the data collection protocol adopted in the experiment.

Data for the bench true biases [14]

These are the data needed to find the bench true values considered as a reference in the error analysis.

In this experiment, the IMU is initially mounted on the PA10 in a way that its sensing axes are aligned as much as possible with the navigation frame, so that it is possible to assume the $[\psi, \theta, \phi]$ angles small enough to make the linearization assumption valid and simplify the equations accordingly.

Therefore, the $\hat{\boldsymbol{X}}_{IMU}$ is aligned with the $\hat{\boldsymbol{N}}$ direction and the $\hat{\boldsymbol{Z}}_{IMU}$ with the $\hat{\boldsymbol{U}}$ direction. Moreover, the misalignment definition between the two frames is the one introduced in Figure 3.8. The experimental setup used for the bench true bias evaluation is shown in Figure 4.5.
After the initial alignment, the PA10 robotic arm starts moving in order to save data for each IMU axis $[\hat{\boldsymbol{X}}_{IMU}, \hat{\boldsymbol{Y}}_{IMU}, \hat{\boldsymbol{Z}}_{IMU}]$ being aligned with the $\hat{\boldsymbol{U}}$ direction and, afterward, with the $-\hat{\boldsymbol{U}}$ one.
The IMU was kept static for 120 seconds in each of the following configurations:

- $\hat{\boldsymbol{Z}}_{IMU}$ aligned with $\hat{\boldsymbol{U}}$;
- $\hat{\boldsymbol{Z}}_{IMU}$ aligned with $-\hat{\boldsymbol{U}}$;
- $\hat{\boldsymbol{Y}}_{IMU}$ aligned with $-\hat{\boldsymbol{U}}$;
- $\hat{\boldsymbol{Y}}_{IMU}$ aligned with $\hat{\boldsymbol{U}}$;
- $\hat{\boldsymbol{X}}_{IMU}$ aligned with $-\hat{\boldsymbol{U}}$;
- $\hat{\boldsymbol{X}}_{IMU}$ aligned with $\hat{\boldsymbol{U}}$;

These static intervals provide the data required to estimate the bench true bias values of the IMU channels, as discussed in Section 5.2. The corresponding inclinometer outputs are shown in Figure 4.6.

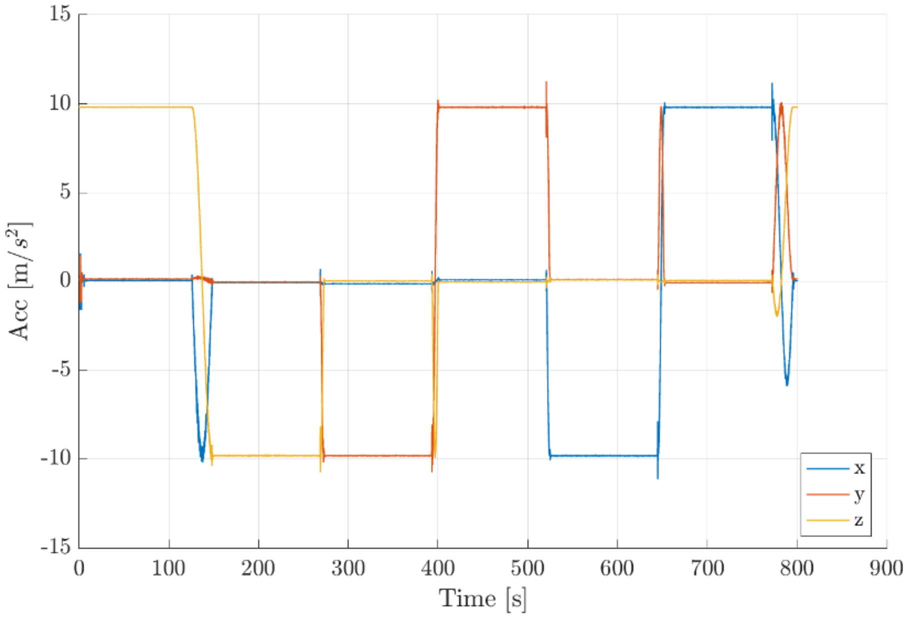

FIGURE 4.6: Inclinometer outputs recorded from the experiment for the estimation of the bias bench true values.

As shown in Section 5.3, the data acquired during the complete 360° rotation (see Figure 4.8) are also used to estimate the interface-to-IMU inclination angles α and β. These angles characterize the mounting misalignment between the interface and the IMU frames and provide the *a priori* alignment values used in the real-case calibration procedure described in Chapter 6.

Data to simulate the real-case scenario [11]

The second dataset was collected to simulate the real-case calibration procedure. In this case, the IMU was treated as if it were already mounted on a launcher. Therefore, the calibration procedure was constrained to motions compatible with the mounted configuration, rather than relying on arbitrary repositioning of the sensor. In that way, the auto-calibration and auto-alignment procedures can be validated through real data.

To do that, the STIM300 is:

– maintained static for 10 minutes with its $\hat{\boldsymbol{Z}}_{IMU}$ directed along the $\hat{\boldsymbol{U}}$ direction. This dataset provides the static measurements used to estimate the pitch θ and roll ϕ angles and to support the accelerometer bias estimation, as described in Section 6.2. The corresponding inclinometer outputs are shown in Figure 4.7;

– rotated four times by 90° around the vertical direction, while maintaining the $\hat{\boldsymbol{Z}}_{IMU}$ axis approximately aligned with $\hat{\boldsymbol{U}}$. After each 90° rotation, the IMU was kept static for 120 seconds.

  This provided static data at four angular positions, corresponding approximately to rotations of 90°, 180°, 270° and 360° with respect to its initial configuration, that is the one quasi-aligned with the navigation frame. These measurements are used for the inclinometer bias estimation procedure described in Section 6.1;

– rotated of 360° around the vertical direction, with the $\hat{\boldsymbol{Z}}_{IMU}$ axis directed along the $\hat{\boldsymbol{U}}$ direction. The purpose of this dataset was to introduce controlled rotational excitation and to provide the additional information required to separate gyroscope bias effects from yaw-related misalignment effects. This dataset is analyzed in Section 6.3. The gyro outputs recorded during the full rotation are shown in Figure 4.8.

  Unfortunately, it is not possible to input a specific speed for the PA10. In fact, it automatically reaches a constant velocity once the starting and the ending points have been imposed.

  It should be noted that the mathematical framework developed in Chapter 6 is presented assuming a counterclockwise rotation as the reference convention. However, the experimental dataset analyzed in this thesis corresponds to a clockwise rotation around the $-\hat{\boldsymbol{U}}$ direction (see Figure 4.8). Although further experiments were attempted, an anomaly during the IMU warm-up phase occurred, rendering the new data unreliable. This introduces sign changes in the equations associated with the rotational motion. The sign changes are taken into account in the implementation used for the data analysis, while the theoretical derivation is kept in the counterclockwise convention for clarity.

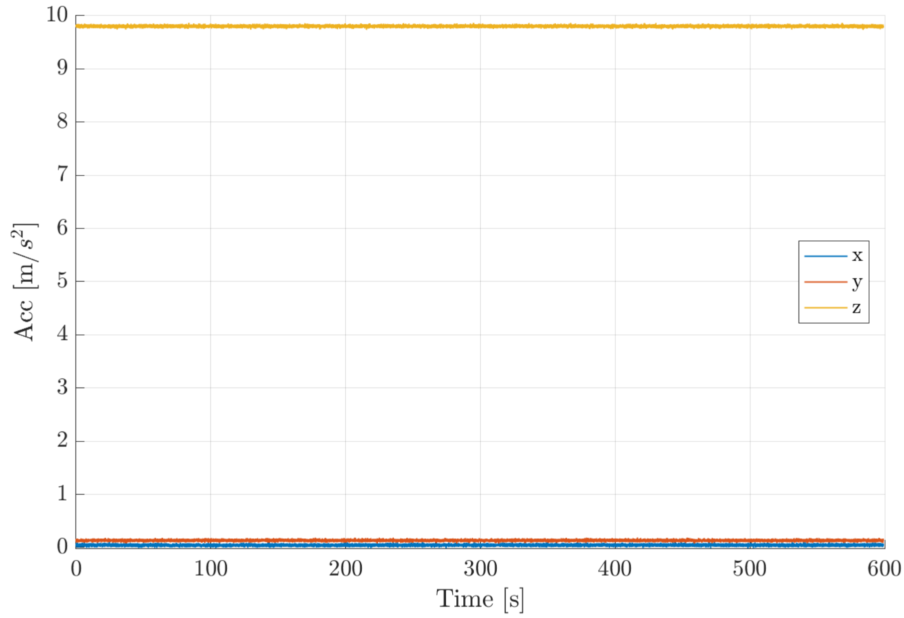

FIGURE 4.7: Inclinometer outputs for the 10 minutes during which the IMU is static with $\hat{\boldsymbol{Z}}_{IMU}$ along the $\hat{\boldsymbol{U}}$ direction.

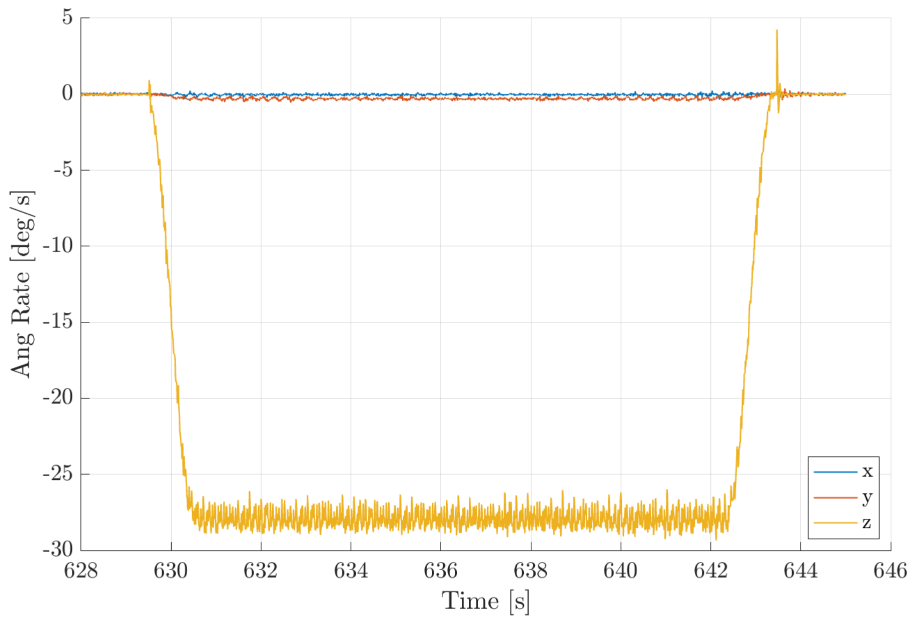

FIGURE 4.8: Gyroscope outputs during the 360° rotation around the $-\hat{\boldsymbol{U}}$ direction. This plot also includes the acceleration and deceleration ramps.

The complete set of data described in this section is used to estimate the IMU biases and the rotation matrix R_{NAV}^{IMU}. The final estimated parameters and their comparison with the bench true values are reported in Chapter 7.

CHAPTER 5

Laboratory Calibration

5.1 Warm-up phase

Before any calibration data is recorded, the STIM300 IMU is powered on and left warming up for at least 1 hour and 30 minutes.

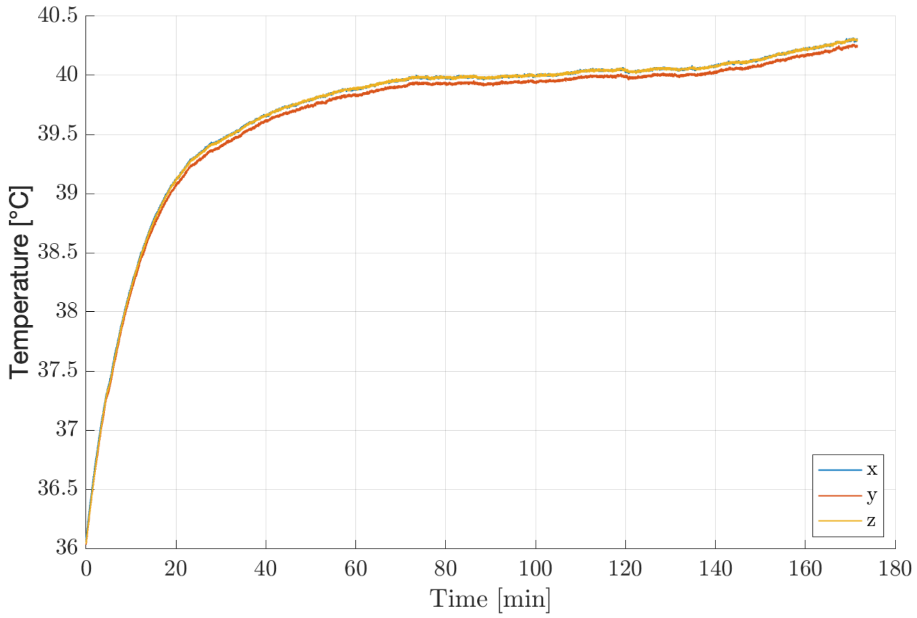

FIGURE 5.1: Accelerometer temperature variation during the 3 hours warm-up interval after STIM300 power-on.

This preliminary phase was included to allow the sensor temperature to reach a more stable condition before starting the experimental procedures.

Since inertial sensor outputs are affected by temperature-dependent effects, performing the calibration after a warm-up interval reduces the influence of thermal transients on the estimated bias values [14, 13].

Figure 5.1 shows the temperature [°C] variation measured on the accelerometer channels during a 3 hours warm-up interval after the IMU is powered on. As shown in the Figure, the temperature increases during the first part of the acquisition and then tends toward a more stable behavior. The inclinometer and gyroscope temperature measurements follow a similar trend.

For this reason, the calibration experiments described in this Chapter and in Chapter 6 are performed only after the initial warm-up phase, so that the estimated bias values are not dominated by the transient thermal behavior of the sensor.

5.2 Bench True Biases

This section describes the procedure used to compute the bench true bias values of the STIM300 IMU. These values are later used as reference quantities to evaluate the accuracy of the real-case calibration procedure (see Chapter 7). The adopted procedure is based on the internal methodology developed at GMV and reported in [14, 16], and it is related to gravity-based and multi-position IMU calibration approaches discussed in the literature [4, 5].

As described in Section 4.2, the PA10 robotic arm was programmed to place the IMU in different static orientations. In each configuration, one IMU sensing axis was aligned as accurately as possible with the vertical direction $\hat{\boldsymbol{U}}$ of the navigation frame and then with the opposite direction $-\hat{\boldsymbol{U}}$.
The IMU was kept static for 120 seconds in each position, so that the recorded data could be averaged to reduce the effect of white noise, as discussed in Section 3.2.2. The complete sequence of static orientations can be observed from the inclinometer outputs shown in Figure 4.6.

The objective of this procedure is to estimate the sensor bias by exploiting measurements acquired in opposite orientations. When the same sensing axis is aligned once with $\hat{\boldsymbol{U}}$ and once with $-\hat{\boldsymbol{U}}$, the gravity-related contribution changes sign, while the bias can be assumed approximately constant. Therefore, by summing the two averaged measurements, the gravity contribution is canceled and the bias term can be isolated.

To clarify the procedure, the derivation of the accelerometer bias along the $\hat{\boldsymbol{X}}_{\boldsymbol{IMU}}$ axis is reported in the following. The same approach is then applied to the other accelerometer, inclinometer and gyroscope channels.

Although the derivation is written for the accelerometer bias, Figures 5.2 and 5.3 show the corresponding inclinometer outputs for the same two static configurations. The inclinometer signals are used here only for illustrative purposes, because they are less noisy and make the change of sign of the gravity-related contribution more clearly visible.

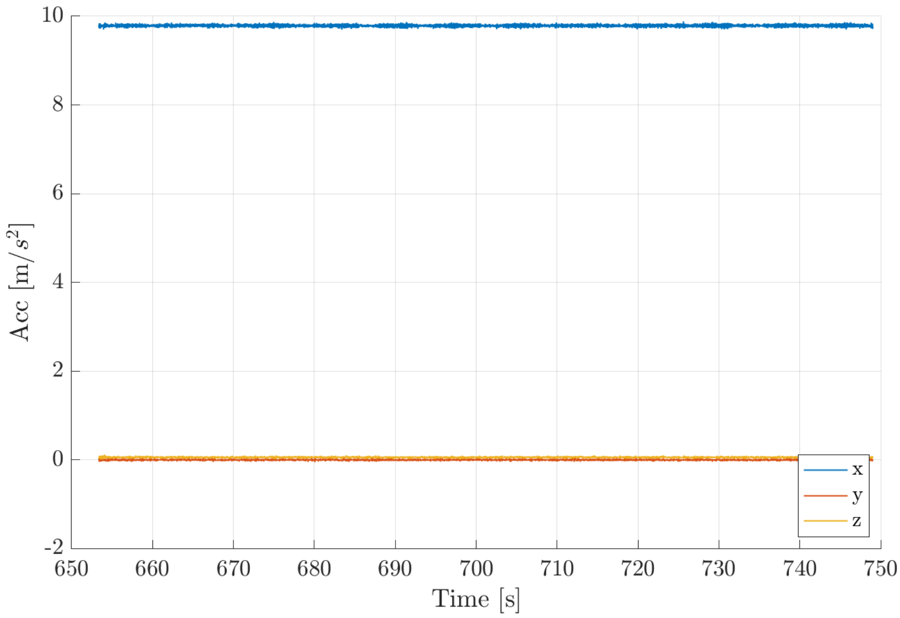

FIGURE 5.2: Inclinometer outputs when the IMU is placed with its X-channel pointing the $\hat{\boldsymbol{U}}$ direction of the navigation frame.

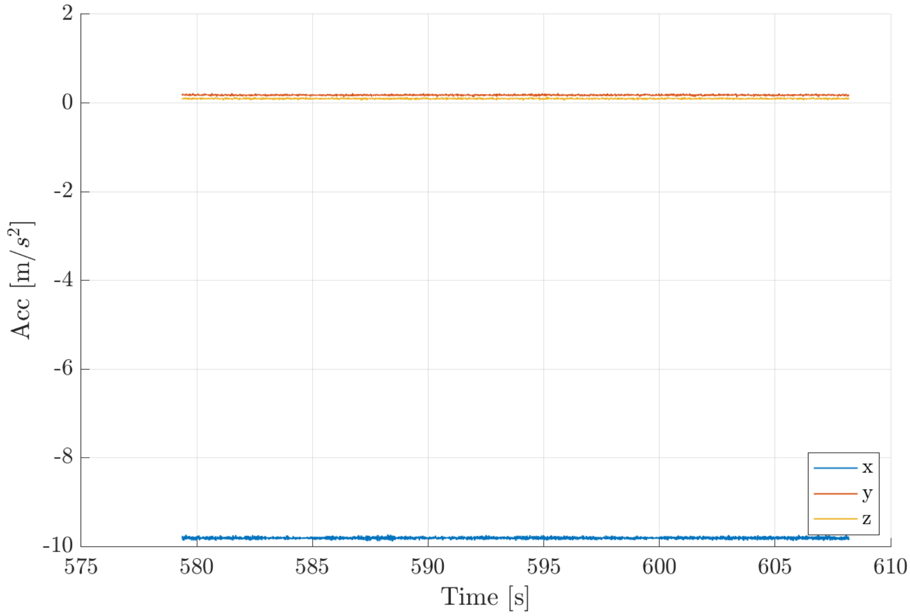

FIGURE 5.3: Inclinometer outputs when the IMU is placed with its X-channel pointing the $-\hat{\boldsymbol{U}}$ direction of the navigation frame.

The static intervals corresponding to the two configurations are selected, and the mean values of the $\hat{\boldsymbol{X}}_{IMU}$ accelerometer output are computed. These averaged values are denoted as $\mathbf{X}_{Up}$ and $\mathbf{X}_{Down}$.

Under the assumption of small residual misalignment between the selected IMU axis and the vertical direction of the navigation frame, the two averaged measurements represent the sensed acceleration in the IMU frame, that is the reaction force of the local gravitational acceleration $\mathbf{f}_{IMU} = -\mathbf{g}_0$, plus the intrinsic bias of the X-channel $\mathbf{b}^a_X$.
Hence

$$\mathbf{X}_{Up} = g_0 \cdot \hat{\boldsymbol{U}} + \mathbf{b}^a_X \tag{5.1}$$

and

$$\mathbf{X}_{Down} = -g_0 \cdot \hat{\boldsymbol{U}} + \mathbf{b}^a_X \tag{5.2}$$

By summing Equations 5.1 and 5.2, the gravity contribution is removed and the accelerometer bias of the X-channel can be estimated as

$$\mathbf{b}^a_X = \frac{1}{2}(\mathbf{X}_{Up} + \mathbf{X}_{Down}) \tag{5.3}$$

This method is applied to all the accelerometer channels by considering the corresponding pairs of opposite static orientations. The same principle is also used to estimate the bench true bias values of the inclinometers, since they also provide gravity-related inclination measurements under static conditions. For the gyroscopes, the estimation procedure is based on the same averaging principle, but the physical reference is the Earth rotation vector $\boldsymbol{\Omega}_E$ rather than the gravity vector. The Earth rotation vector expressed in the navigation frame is defined in Equation 4.2. In static conditions, the measured angular rate is composed of the projection of this vector onto the IMU axes and the gyroscope bias, as expressed in Equation 6.21.

It is important to compute the bench true bias values from the same experimental campaign used for the subsequent validation. Indeed, the bias value may change between different sensor activations due to turn-on bias variation, as discussed in Chapter 2 and Section 3.2.1.
For this reason, the bench true values obtained in this section are used as reference values for the comparison with the parameters estimated in the real-case procedure described in Chapter 6.
The bench true bias values computed through this method are reported in the Table 5.1 below.

Bench True	**X-channel**	**Y-channel**	**Z-channel**
INC Bias [mg]	-0.8990	-0.6567	-0.2351
ACC Bias [mg]	-1.2811	7.0304	0.5056
GYRO Bias [$^{\circ}/_{h}$]	98.6017	-34.7380	-27.4377

TABLE 5.1: Bench true bias values obtained from the laboratory calibration procedure.

5.3 Interface Inclination: Computation of α and β

To perform the real-case calibration procedure described in Chapter 6, the interface-to-IMU misalignment angles α and β must be characterized. These

angles describe the relative orientation between the interface frame and the IMU frame, as introduced in Section 3.1 and shown in Figure 3.7.
Throughout this thesis, the interface-to-IMU misalignment angles α and β are assumed to be characterized in laboratory conditions and are therefore treated as *a priori* values in the real-case calibration procedure. This distinction is important because the datasets used to estimate α and β are different from the dataset used in Chapter 6 to validate the real-case auto-calibration and auto-alignment procedure. In this way, α and β represent parameters determined before the operational calibration phase, that is before considering the IMU mounted on the launcher.

The general mathematical framework adopted in this work is based on the internal methodology reported in [17, 12, 14]. Within this framework the explicit estimation of the interface-to-IMU misalignment angles α and β was introduced in this thesis after observing the sensitivity of the gyroscope-based estimation to these parameters.
In fact, although α and β are small, they determine how the angular velocity imposed by the robotic arm is projected onto the IMU axes. This is the reason why this type of misalignment cannot be properly identified from static data alone, its effect becomes observable only when a rotational motion is imposed and the corresponding angular rate contribution is measured by the gyroscopes. Therefore, neglecting α and β would introduce residual components in the gyroscope measurements after the robot angular rate is removed and, consequently, an error in the gyroscope bias estimation, as will be discussed in Section 7.1.

The full matrix describing the alignment between the interface frame and the IMU frame is built through a composition of Euler rotations, according to the 3-2-1 rotation convention introduced in Section 3.1.
The rotation from the interface frame to the IMU frame is described by the matrix R_{int}^{IMU} and it is written as

$$R_{int}^{IMU} = R_1(\alpha) \cdot R_2(\beta) \cdot R_3(0) \tag{5.4}$$

so, the complete matrix is

$$R_{int}^{IMU} = \begin{bmatrix} \cos(\beta) & 0 & -\sin(\beta) \\ \sin(\alpha)\sin(\beta) & \cos(\alpha) & \sin(\alpha)\cos(\beta) \\ \cos(\alpha)\sin(\beta) & -\sin(\alpha) & \cos(\alpha)\cos(\beta) \end{bmatrix} \tag{5.5}$$

The mean values observed on the $\hat{\boldsymbol{X}}_{IMU}$ and $\hat{\boldsymbol{Y}}_{IMU}$ gyroscope channels cannot be attributed only to the nominal gyroscope bias. Indeed, as can be seen from Figure 5.4, these components are larger than the expected gyroscope bias level from the STIM300 specifications [13], especially the one of the Y-channel. They are therefore interpreted as the effect of the interface-to-IMU misalignment, which introduces constant angular rate contributions on the lateral IMU channels during the robot rotation.

The effect of this misalignment becomes evident when analyzing the gyroscope data acquired during the complete 360° rotation described in Section 4.2. During this motion, the angular rate imposed by the robot ($\boldsymbol{\omega}_{Rob}$) is mainly aligned with the vertical direction of the interface. If the interface frame and the IMU frame were perfectly aligned, this contribution would mainly appear on the $\hat{\boldsymbol{Z}}_{IMU}$ gyroscope channel. However, because of the small interface-to-IMU misalignment, part of $\boldsymbol{\omega}_{Rob}$ is projected onto the $\hat{\boldsymbol{X}}_{IMU}$ and $\hat{\boldsymbol{Y}}_{IMU}$ channels.

Before attributing these components to α and β, all the other relevant contributions must be removed from the gyroscope outputs. In particular, the bench true gyroscope biases computed in Section 5.2 are subtracted, and the contribution of the Earth rotation vector is removed. This removal requires the attitude angles describing the navigation-to-IMU misalignment, namely pitch θ, roll ϕ, and yaw ψ. These angles are needed to correctly express $\boldsymbol{\Omega}_E$ in the IMU frame and are computed below.

Therefore, the estimation of α and β relies on two distinct levels of alignment. The navigation-to-IMU angles ψ, θ, and ϕ are used to remove the $\boldsymbol{\Omega}_E$ contribution from the measured gyroscope outputs. Once this contribution, together with the gyroscope biases, has been removed, the remaining angular rate signal is associated with the robot rotation $\boldsymbol{\Omega}_{Rob}$. The interface-to-IMU angles α and β are then obtained from the robot angular rate projections onto the IMU axes.

This analysis motivates the explicit computation of α and β, whose values are reported in Table 5.2.

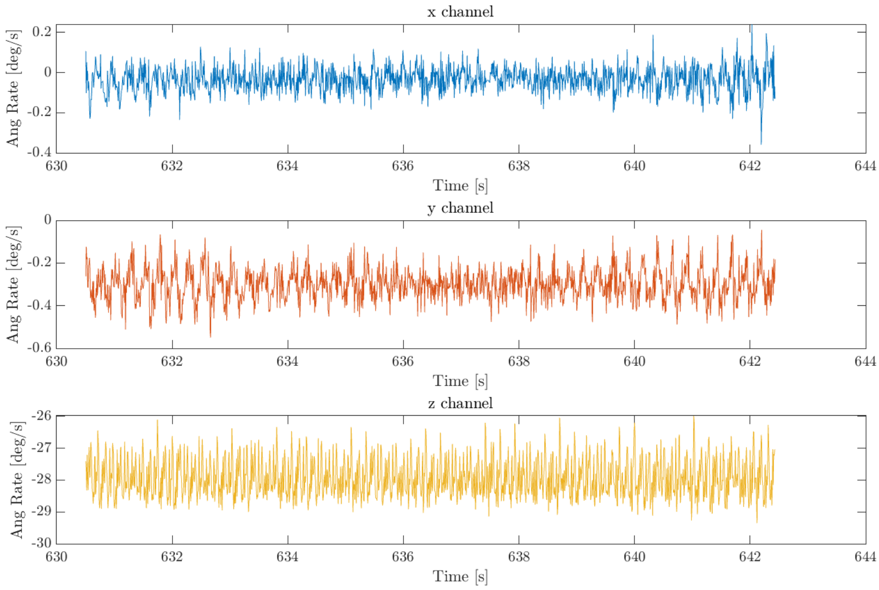

FIGURE 5.4: Gyroscope outputs during the complete 360° rotation. The non-zero mean values observed on the X- and Y-channels indicate that the robot angular velocity is projected onto the IMU axes.

The computation of α and β is performed after the NAV–IMU misalignment is obtained. Therefore, a preliminary analysis is conducted to obtain θ and ϕ from the same equations used in Section 6.2, by using the bench true biases. These angles are required to remove the Earth rate contribution from the gyroscope outputs. Hence, all the contributions not related to α and β are removed from the gyro outputs and the angles can be estimated.
The whole procedure to estimate the $\boldsymbol{\omega}_{Rot}^{NB}$ vector is explained below, where $\boldsymbol{\omega}_{Rot}^{NB}$ is the angular velocity of the robot obtained after removing all the effects mentioned above.

The equations for the gyroscope outputs during the rotation are derived in Section 6.3 and are here written for simplicity:

$$
\begin{aligned}
\boldsymbol{\omega}_{IMU} = \begin{bmatrix} \omega_X^{IMU} \\ \omega_Y^{IMU} \\ \omega_Z^{IMU} \end{bmatrix} \approx \begin{bmatrix} \Omega_E \cos(\lambda) - \theta \cdot \Omega_E \sin(\lambda) \\ -\psi(t) \cdot \Omega_E \cos(\lambda) + \phi \cdot \Omega_E \sin(\lambda) \\ \theta \cdot \Omega_E \cos(\lambda) + \Omega_E \sin(\lambda) \end{bmatrix} + \\
+ \begin{bmatrix} -\sin(\beta) \cdot \omega_{Rob} \\ \sin(\alpha)\cos(\beta) \cdot \omega_{Rob} \\ \cos(\alpha)\cos(\beta) \cdot \omega_{Rob} \end{bmatrix} + \begin{bmatrix} b_X^{\omega} \\ b_Y^{\omega} \\ b_Z^{\omega} \end{bmatrix}
\end{aligned}
\tag{5.6}
$$

Then, after canceling out biases and $\boldsymbol{\Omega}_E$ contributions due to θ and ϕ, the following is obtained

$$
\begin{aligned}
\boldsymbol{\omega}_{IMU} = \begin{bmatrix} \omega_X^{IMU} \\ \omega_Y^{IMU} \\ \omega_Z^{IMU} \end{bmatrix} - \begin{bmatrix} \Omega_E \cos(\lambda) - \theta \cdot \Omega_E \sin(\lambda) \\ \phi \cdot \Omega_E \sin(\lambda) \\ \theta \cdot \Omega_E \cos(\lambda) + \Omega_E \sin(\lambda) \end{bmatrix} - \begin{bmatrix} b_X^{\omega} \\ b_Y^{\omega} \\ b_Z^{\omega} \end{bmatrix} = \\
= \begin{bmatrix} -\sin(\beta) \cdot \omega_{Rob} \\ \sin(\alpha)\cos(\beta) \cdot \omega_{Rob} - \psi(t) \cdot \Omega_E \cos(\lambda) \\ \cos(\alpha)\cos(\beta) \cdot \omega_{Rob} \end{bmatrix}
\end{aligned}
\tag{5.7}
$$

Equation 5.7 shows more explicitly why a rotation is required to estimate α and β. These angles appear through the projection of $\boldsymbol{\omega}_{Rob}$ onto the IMU axes. Without the robot angular velocity, the terms containing α and β would not provide an independent observable contribution in the gyroscope outputs. In other words, the interface-to-IMU misalignment is identified from the rotational excitation, while the NAV–IMU misalignment angles are used to remove the Earth rate contribution.
By averaging Equation 5.7 over the complete rotation, the contribution due to the $\psi(t)$ angle cancels out and α and β can be evaluated:

$$\alpha = \operatorname{atan2}\left({}^{\omega^{NB}_{Rot_Y}} / {}_{\omega^{NB}_{Rot_Z}} \right) \tag{5.8a}$$

$$\beta = -\operatorname{atan2}\left({}^{\omega^{NB}_{Rot_X}} / {}_{\omega^{NB}_{Rot_Z}} \right) \tag{5.8b}$$

With the purpose of addressing this problem in the most general form, all the procedure explained above is applied for different sets of rotation data that have been collected in the laboratory.
In the end, a mean is applied to derive the angles α and β, which will be used as *a priori* values.
They are shown below

$\boldsymbol{\alpha}$ [°]	$\boldsymbol{\beta}$ [°]
0.5964	-0.1125

Table 5.2: Nominal laboratory interface-to-IMU misalignment angles used as *a priori* values in the real-case procedure.

Although these laboratory values were considered qualitatively good, their accuracy was not sufficient to correctly evaluate the yaw angle ψ and, as a consequence, the gyroscope bias of the Y-channel, as discussed in Section 7.1. Indeed, if α and β are evaluated using the set of data collected for the real-case experiment of Section 6.3, they appear to be

$\boldsymbol{\alpha}$ [°]	$\boldsymbol{\beta}$ [°]
0.5934	-0.1196

Table 5.3: Same-dataset interface-to-IMU misalignment angles used for the sensitivity analysis.

The values reported in Table 5.2 are used as *a priori* parameters in the nominal real-case calibration procedure described in Chapter 6. Conversely, the values reported in Table 5.3 are computed from the same rotation dataset used in Section 6.3. They are not used in the nominal procedure, but are introduced to assess the sensitivity of the gyroscope-based yaw estimation to the accuracy of the interface-to-IMU misalignment angles in Section 7.1.

Although the difference between Tables 5.2 and 5.3 is small, its effect can become non-negligible when the projection of $\boldsymbol{\omega}_{Rob}$ is removed from the gyroscope outputs. The effect of using the dataset-specific values of Table 5.3 is analyzed in Section 7.1.

CHAPTER 6

Real-Case Scenario

This chapter presents the experimental and mathematical procedure used to automatically calibrate and align the STIM300 IMU in a configuration representative of a real operational scenario. Unlike the laboratory calibration described in Chapter 5, the IMU is here treated as already mounted on a rotary platform. Therefore, it cannot be freely repositioned to perform the complete set of orientations required for the bench true bias estimation described in Section 5.2.
The objective of the real-case procedure is to estimate the relevant sensor biases and the misalignment angles between the navigation frame and the IMU frame by exploiting the data collected during the mounted IMU experiment described in Section 4.2. In particular, the procedure uses both static intervals and controlled rotations around the approximately vertical $\hat{\boldsymbol{Z}}_{IMU}$ axis. This makes it possible to reproduce the constraints of a sensor installed on a launcher or final platform, where only limited rotational motion is available.

The procedure developed in this chapter relies on the following key assumptions:

- The interface-to-IMU misalignment angles α and β are small and known (Table 5.2). They are treated as *a priori* values, obtained from the laboratory characterization described in Section 5.3. Their accuracy is essential for the gyroscope-based estimation, as discussed in Section 7.1;
- The Z-axis inclinometer bias is assumed to be negligible: $b^i_Z = 0$. This assumption is introduced because the experimental motion used in this section does not provide enough information to independently estimate the Z-axis inclinometer bias, and it is very small (see Table 5.1);
- All Euler angles involved in the procedure are assumed to be small. Therefore, linearized rotation matrices can be always used;

- Before starting the calibration procedure, the IMU is warmed-up for at least 1 hour and 30 minutes, as described in Section 5.1. This reduces the influence of the initial thermal transient on the estimated bias values.

The IMU calibration experiment, performed to simulate a real-case scenario and carried out using the PA10 robotic arm, is conducted following the subsequent steps.
First, the inclinometer biases are estimated using four static positions obtained after successive 90° rotations around the vertical direction. This step is described in Section 6.1.
Then, the estimated inclinometer biases are removed from the static inclinometer measurements to compute the pitch θ and roll ϕ angles and to estimate the accelerometer biases, as described in Section 6.2.
Finally, both the gyroscope static measurements and the ones acquired during the complete 360° rotation are used to estimate the gyroscope biases and the yaw angle ψ, as discussed in Section 6.3.

The final estimated parameters and the additional sensitivity analyses are reported in Chapter 7, while the main limitations and possible improvements of the methodology are discussed in Chapter 8.

6.1 Inclinometers Bias Estimation

The first step of the real-case calibration procedure consists in estimating the inclinometer biases. This step is required because the inclinometer measurements are later used to compute the pitch θ and roll ϕ angles, as described in Section 6.2. Therefore, any inclinometer bias would directly affect the attitude estimation and, consequently, the accelerometer bias estimation.

As discussed above, a real mounted IMU cannot be freely repositioned to perform all the orientations required by the bench true bias procedure described in Section 5.2. Hence, a dedicated method is needed to estimate the inclinometer biases while keeping the IMU mounted with the same alignment, using only the available rotary platform.

The mathematical formulation adopted in this section is based on the internal GMV methodology reported in [18]. However, in the present thesis the method is applied in a different experimental context.

The adopted procedure is based on the following experimental sequence:

- The IMU is placed in four static positions, each obtained after a 90° rotation around the $\hat{\boldsymbol{Z}}_{IMU}$ axis, with this axis remaining approximately aligned with the $\hat{\boldsymbol{U}}$ direction of the navigation frame;
- At each position, the IMU is kept static for 120 seconds (see Figure 6.2);
- The outputs of the $\hat{\boldsymbol{X}}_{IMU}$ and $\hat{\boldsymbol{Y}}_{IMU}$ inclinometer channels are analyzed to estimate their biases.

The gyroscope outputs recorded during the four 90° rotations are shown in Figure 6.1. The static intervals used for the inclinometer bias estimation correspond to the portions in which the gyroscope outputs are approximately zero, after each rotation. The different static positions occupied by the IMU are schematically represented in Figure 6.2.

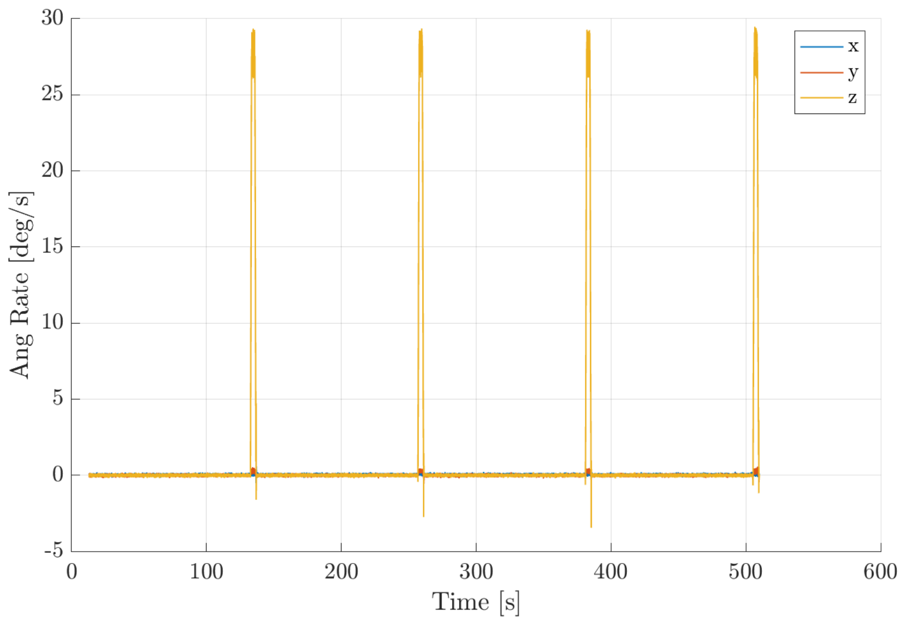

FIGURE 6.1: Gyroscope outputs during the four 90° rotations. The approximately constant portions correspond to the 120 seconds static intervals used for the inclinometer bias estimation.

The objective of the procedure is to exploit the change in the relative orientation between the IMU and the navigation frame during the four positions. Since the rotations are performed around the approximately vertical axis, the gravity contribution measured by the $\hat{\boldsymbol{X}}_{IMU}$ and $\hat{\boldsymbol{Y}}_{IMU}$ inclinometer channels changes from one position to another. By combining the four static measurements, the terms depending on the navigation-to-interface misalignment can be canceled, allowing the inclinometer biases to be isolated.

The following measurement model is applied to the inclinometer outputs. It represents the projection of the gravity reaction force expressed in the navigation frame $\mathbf{f}^i_{NAV} = g_0\,\hat{\mathbf{U}}$ onto the IMU frame

$$\mathbf{f}^i_{IMU} = R^{IMU}_{int} \cdot R^{int}_{NAV} \cdot \mathbf{f}^i_{NAV} + \mathbf{b}^i$$

The computation takes into account the composition of two rotations. The first one is the rotation from the navigation frame to the interface frame described by R^{int}_{NAV} and by the angles $[\gamma_1, \gamma_2, \gamma_3]$, introduced in Figure 3.5. The second one is the rotation from the interface frame to the IMU frame, described by R^{IMU}_{int} and by the angles $[\alpha, \beta, 0]$, introduced in Figure 3.7 and characterized in Section 5.3.

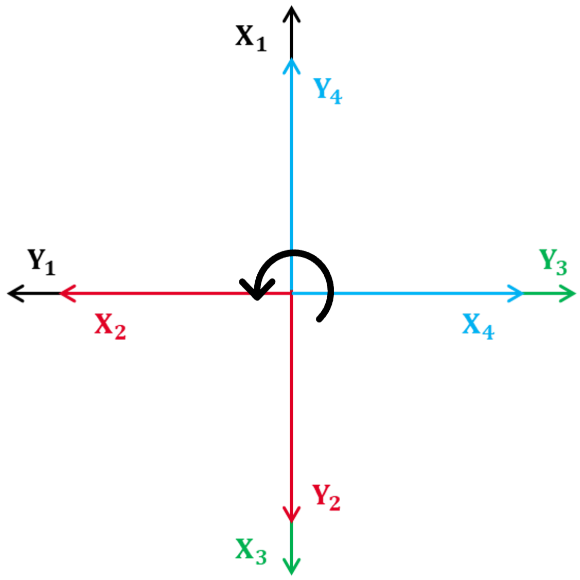

FIGURE 6.2: Scheme of the different positions occupied by the IMU during the inclinometer biases calibration in the laboratory.

The rotation matrix from the interface frame to the IMU frame is

$$R^{IMU}_{int} = R_1(\alpha) \cdot R_2(\beta) \cdot R_3(0) \tag{6.1}$$

$$R_{int}^{IMU} = \begin{bmatrix} \cos(\beta) & 0 & -\sin(\beta) \\ \sin(\alpha)\sin(\beta) & \cos(\alpha) & \sin(\alpha)\cos(\beta) \\ \cos(\alpha)\sin(\beta) & -\sin(\alpha) & \cos(\alpha)\cos(\beta) \end{bmatrix} \tag{6.2}$$

The rotation matrix from the navigation frame to the interface frame is

$$R_{NAV}^{int} = R_1(\gamma_3) \cdot R_2(\gamma_2) \cdot R_3(\gamma_1) \tag{6.3}$$

$$R_{NAV}^{int} = \begin{bmatrix} \cos(\gamma_2)\cos(\gamma_1) & \cos(\gamma_2)\sin(\gamma_1) & -\sin(\gamma_2) \\ -\cos(\gamma_2)\sin(\gamma_1) + \sin(\gamma_3)\sin(\gamma_2)\cos(\gamma_1) & \cos(\gamma_3)\cos(\gamma_1) + \sin(\gamma_3)\sin(\gamma_2)\sin(\gamma_1) & \sin(\gamma_3)\cos(\gamma_2) \\ \sin(\gamma_3)\sin(\gamma_1) + \cos(\gamma_3)\sin(\gamma_2)\cos(\gamma_1) & -\sin(\gamma_3)\cos(\gamma_1) + \cos(\gamma_3)\sin(\gamma_2)\sin(\gamma_1) & \cos(\gamma_3)\cos(\gamma_2) \end{bmatrix} \tag{6.4}$$

Since the angles γ_1, γ_2, and γ_3 are assumed to be small, the matrix R_{NAV}^{int} can be linearized as

$$R_{NAV}^{int} \approx \begin{bmatrix} 1 & \gamma_1 & -\gamma_2 \\ -\gamma_1 & 1 & \gamma_3 \\ \gamma_2 & -\gamma_3 & 1 \end{bmatrix} \tag{6.5}$$

Therefore, the full matrix, multiplied by $\mathbf{f}_{NAV}^{i} = [0, 0, g_0]$ is

$$R_{int}^{IMU} \cdot R_{NAV}^{int} \cdot \mathbf{f}_{NAV}^{i} = \begin{bmatrix} -\gamma_2\ \cos(\beta) \cdot g_0 - \sin(\beta) \cdot g_0 \\ -\gamma_2\ \sin(\alpha)\sin(\beta) \cdot g_0 + \gamma_3\ \cos(\alpha) \cdot g_0 + \sin(\alpha)\cos(\beta) \cdot g_0 \\ -\gamma_2\ \cos(\alpha)\sin(\beta) \cdot g_0 - \gamma_3\ \sin(\alpha) \cdot g_0 + \cos(\alpha)\cos(\beta) \cdot g_0 \end{bmatrix} \tag{6.6}$$

and the gravity reaction force expressed in the IMU frame becomes

$$\mathbf{f}_{IMU}^{i} = R_{int}^{IMU} \cdot R_{NAV}^{int} \cdot \mathbf{f}_{NAV}^{i} + \mathbf{b}^{i} \tag{6.7}$$

Only the $\hat{\boldsymbol{X}}_{IMU}$ and $\hat{\boldsymbol{Y}}_{IMU}$ inclinometer biases are estimated with this method. The Z-axis inclinometer bias remains constant during the four positions because

the rotations are performed around the $\hat{\boldsymbol{Z}}_{IMU}$ axis. Therefore, this procedure does not provide independent information to estimate b^i_Z. Nevertheless, it can be seen that assuming it to be zero introduces only a small error in the computation of the accelerometer biases (see Table 7.6).
For this reason, the following assumption is adopted: $\mathbf{b}^i_Z = 0$.

The matrix product shown in Equation 6.6 refers to the first static position, in which the $\hat{\boldsymbol{X}}_{IMU}$ and $\hat{\boldsymbol{Y}}_{IMU}$ axes are directed along the X_1 and Y_1 directions represented in Figure 6.2.
Here, the inclinometer outputs appear to be:

$$\begin{cases} f^i_{X_1} = -\gamma_2 \cos(\beta)\, g_0 - \sin(\beta)\, g_0 + b^i_X \\ f^i_{Y_1} = -\gamma_2 \sin(\alpha)\sin(\beta)\, g_0 + \gamma_3 \cos(\alpha)\, g_0 + \sin(\alpha)\cos(\beta)\, g_0 + b^i_Y \end{cases} \tag{6.8}$$

Considering the four positions obtained after successive 90° rotations, the following equations are obtained for the $\hat{\boldsymbol{X}}_{IMU}$ and $\hat{\boldsymbol{Y}}_{IMU}$ inclinometer channels:

$$\begin{cases} f^i_{X_2} = -\gamma_3 \cos(\beta)\, g_0 - \sin(\beta)\, g_0 + b^i_X \\ f^i_{Y_2} = -\gamma_3 \sin(\alpha)\sin(\beta)\, g_0 - \gamma_2 \cos(\alpha)\, g_0 + \sin(\alpha)\cos(\beta)\, g_0 + b^i_Y \end{cases} \tag{6.9}$$

$$\begin{cases} f^i_{X_3} = \gamma_2 \cos(\beta)\, g_0 - \sin(\beta)\, g_0 + b^i_X \\ f^i_{Y_3} = \gamma_2 \sin(\alpha)\sin(\beta)\, g_0 - \gamma_3 \cos(\alpha)\, g_0 + \sin(\alpha)\cos(\beta)\, g_0 + b^i_Y \end{cases} \tag{6.10}$$

$$\begin{cases} f^i_{X_4} = \gamma_3 \cos(\beta)\, g_0 - \sin(\beta)\, g_0 + b^i_X \\ f^i_{Y_4} = \gamma_3 \sin(\alpha)\sin(\beta)\, g_0 + \gamma_2 \cos(\alpha)\, g_0 + \sin(\alpha)\cos(\beta)\, g_0 + b^i_Y \end{cases} \tag{6.11}$$

By summing the four $\hat{\boldsymbol{X}}_{IMU}$ channel equations, the terms depending on γ_2 and γ_3 cancel out. Similarly, by summing the four $\hat{\boldsymbol{Y}}_{IMU}$ channel equations, the terms depending on γ_2 and γ_3 also cancel out:

$$f^i_{X_1} + f^i_{X_2} + f^i_{X_3} + f^i_{X_4} = 4\,(-\sin(\beta)\, g_0 + b^i_X) \tag{6.12a}$$

$$f^i_{Y_1} + f^i_{Y_2} + f^i_{Y_3} + f^i_{Y_4} = 4\,(\sin(\alpha)\cos(\beta)\, g_0 + b^i_Y) \tag{6.12b}$$

The inclinometer biases can therefore be estimated as

$$b^i_X = \frac{f^i_{X_1} + f^i_{X_2} + f^i_{X_3} + f^i_{X_4}}{4} + \sin(\beta)\, g_0 \tag{6.13a}$$

$$b^i_Y = \frac{f^i_{Y_1} + f^i_{Y_2} + f^i_{Y_3} + f^i_{Y_4}}{4} - \sin(\alpha)\cos(\beta)\, g_0 \tag{6.13b}$$

Therefore, the computed inclinometer bias vector is $\boldsymbol{b}^i = [b^i_X, b^i_Y, 0]$. The numerical values and their comparison with the bench true values are reported in Table 7.5.

The subsequent step consists in subtracting these bias values from the static inclinometer outputs acquired with the IMU kept still for 10 minutes and with the $\hat{\boldsymbol{Z}}_{IMU}$ axis approximately aligned with the $\hat{\boldsymbol{U}}$ direction.
This allows a more accurate estimation of the pitch θ and roll ϕ angles, and consequently improves the accelerometer bias estimation. This procedure is described in Section 6.2.

6.2 Pitch and Roll Estimations & Accelerometer Biases

The inclinometer biases estimated with the method described in Section 6.1 are subtracted from the static inclinometer data acquired with the IMU kept still for 10 minutes, with its $\hat{\boldsymbol{Z}}_{IMU}$ axis approximately aligned with the $\hat{\boldsymbol{U}}$ direction of the navigation frame. This static acquisition is shown in Figure 4.7.

At this point, the objective is to estimate the pitch θ and roll ϕ angles, which describe the misalignment between the navigation frame and the IMU frame. These angles are part of the Euler angle set $[\psi, \theta, \phi]$, shown in Figure 3.8.

The complete rotation from the navigation frame to the IMU frame is described by the matrix R^{IMU}_{NAV}. According to the 3-2-1 Euler rotation convention introduced in Section 3.1, this matrix is written as

$$R^{IMU}_{NAV} = R_1(\phi) \cdot R_2(\theta) \cdot R_3(\psi) \tag{6.14}$$

that is Equation 3.2.

With the purpose of evaluating the angles, the reaction force of the gravity vector expressed in the navigation frame $\mathbf{f}_{NAV} = [0, 0, g_0]$, is projected in the IMU frame by means of the rotation matrix R_{NAV}^{IMU}.
After subtracting the inclinometer biases estimated in Section 6.1, the corrected inclinometer outputs can be modeled as

$$\mathbf{f}_{IMU}^{i} = R_{NAV}^{IMU} \cdot \mathbf{f}_{NAV} = \begin{bmatrix} -\sin(\theta) \cdot g_0 \\ \sin(\phi)\cos(\theta) \cdot g_0 \\ \cos(\phi)\cos(\theta) \cdot g_0 \end{bmatrix} \tag{6.15}$$

Equation 6.15 allows the pitch and roll angles to be determined from the corrected inclinometer outputs.
In particular, they are computed as

$$\phi = \operatorname{atan2}\left(\frac{f_Y^i}{f_Z^i}\right) \tag{6.16a}$$

$$\theta = -\operatorname{atan2}\left(\frac{f_X^i \ \cos(\phi)}{f_Z^i}\right) \tag{6.16b}$$

The values of θ and ϕ obtained from the corrected inclinometer outputs are reported in Table 7.7, where they are compared with the corresponding reference values reported in Table 7.4. These reference pitch and roll angles are obtained by applying the same static attitude estimation procedure used in this section, but using the bench true inclinometer bias values computed in laboratory conditions.
These angles are then used to estimate the accelerometer biases from the static accelerometer measurements.

Since the IMU remains static during this acquisition, the accelerometer outputs contain the projection of the gravity reaction force onto the IMU axes and the accelerometer bias vector.
Therefore, the accelerometer measurement model can be written as

$$\mathbf{f}_{IMU}^{a} = R_{NAV}^{IMU} \cdot \mathbf{f}_{NAV} + \mathbf{b}^a = \begin{bmatrix} -\sin(\theta)\, g_0 \\ \sin(\phi)\cos(\theta)\, g_0 \\ \cos(\phi)\cos(\theta)\, g_0 \end{bmatrix} + \begin{bmatrix} b_X^a \\ b_Y^a \\ b_Z^a \end{bmatrix} \tag{6.17}$$

The accelerometer biases $\mathbf{b}^a$ are obtained by subtracting the gravity projection from the static accelerometer outputs and by averaging the remaining signal over the static interval.
Therefore,

$$\begin{cases} b^a_X = f^a_X + \sin(\theta) g_0 \\ b^a_Y = f^a_Y - \sin(\phi)\cos(\theta)\, g_0 \\ b^a_Z = f^a_Z - \cos(\phi)\cos(\theta)\, g_0 \end{cases} \tag{6.18}$$

The numerical values of the accelerometer biases obtained through this procedure and their comparison with the bench true values are reported in Table 7.6.
The pitch and roll angles estimated in this section are also required in the following gyroscope analysis, because they are used to express the Earth rotation vector in the IMU frame. The estimation of the gyroscope biases and of the yaw angle ψ is described in Section 6.3.

6.3 Gyro biases & Yaw Angle Estimation

The last step of the real-case calibration procedure consists in estimating the gyroscope biases and the yaw angle ψ. While pitch θ and roll ϕ can be obtained from static inclinometer measurements, as described in Section 6.2, the yaw angle cannot be determined from gravity-based measurements. Indeed, gravity does not provide heading information, and therefore an additional source of information is required.

In this work, the yaw estimation relies on the gyroscope measurements and, in particular, on the capability of the STIM300 gyroscopes to detect the Earth rotation contribution. For this reason, before applying the gyroscopes calibration and alignment procedure, a preliminary analysis is performed to verify that the $\mathbf{\Omega}_E$ is actually observable in the gyroscope data.
The static gyroscope measurements are first processed in order to reduce the effect of high-frequency noise. A Gaussian filter is applied to the measured angular rates, while preserving the low-frequency contribution associated with the Earth rotation. The filtered gyroscope outputs are shown in Figure 6.3.

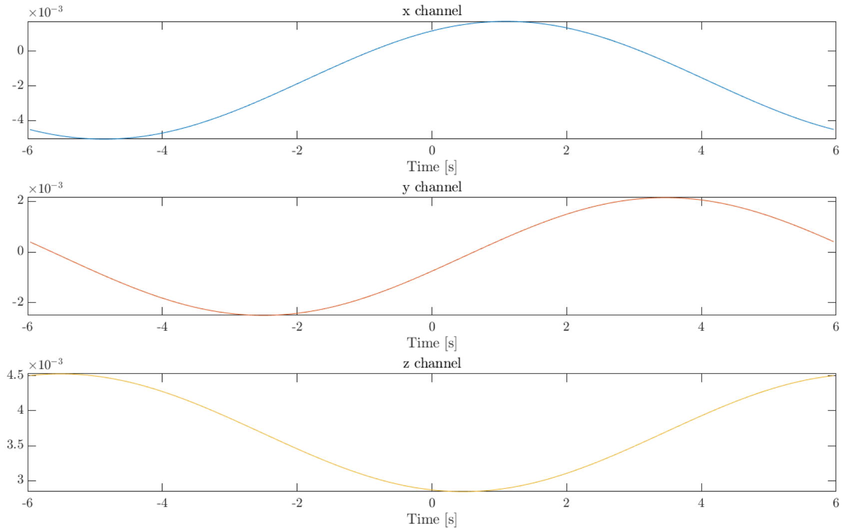

FIGURE 6.3: Plot of the gyro outputs filtered through a Gaussian (mountain) filter.

The filtered gyroscope signal is then analyzed in the frequency domain. The objective of this analysis is not to estimate the calibration parameters directly, but to verify that the gyroscope measurements contain a detectable contribution compatible with the expected Earth rotation rate. The result of the frequency-domain analysis is shown in Figure 6.4.

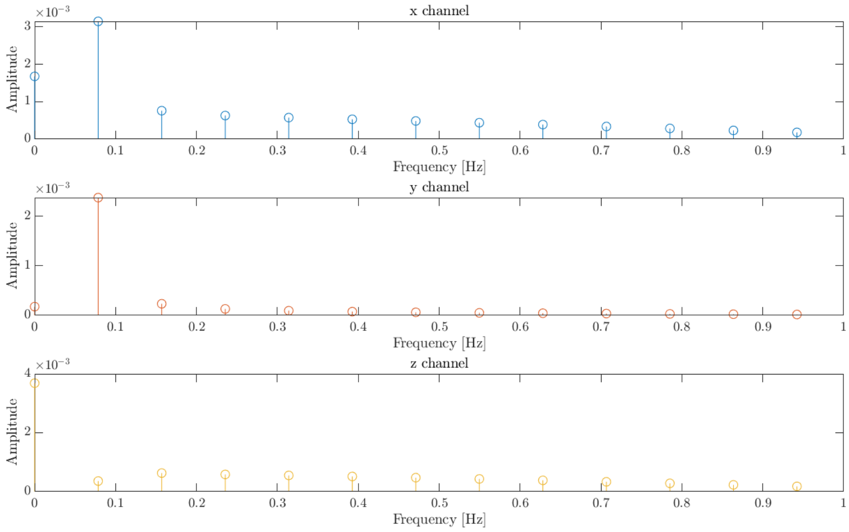

FIGURE 6.4: Frequency-domain analysis of the filtered gyroscope outputs shown in Figure 6.3. Around the frequency associated with the observed oscillation, the Fourier amplitude is of the same order of magnitude as $\Omega_E \cos(\lambda)$, expressed in $°/_s$.

This preliminary analysis confirms that the gyroscope signal contains information at the order of magnitude of the Earth rotation contribution.
This point is important because the yaw estimation performed later in this section depends on the term $\Omega_E \cos(\lambda)$, which is very small. Therefore, the reliability of the yaw estimation is strongly connected to the ability of the sensor to measure such a small angular rate contribution. The frequency domain analysis is used only as a diagnostic tool.

The gyroscope biases and yaw angle are estimated in the time domain using the analytical model derived below.
The vector of the Earth rotation expressed in the navigation frame is here recalled

$$\mathbf{\Omega}_{E_{NAV}} = \begin{bmatrix} \Omega_E \cos(\lambda) \\ 0 \\ \Omega_E \sin(\lambda) \end{bmatrix} \tag{6.19}$$

where λ is the latitude.

Under static conditions, the gyroscope outputs are given by the sum of the

Earth rotation vector projected onto the IMU axes and the gyroscope bias vector

$$\boldsymbol{\omega}_{IMU} = R_{NAV}^{IMU} \cdot \boldsymbol{\Omega}_{E_{NAV}} + \mathbf{b}^{\omega} \tag{6.20}$$

By projecting the Earth rotation vector expressed in the navigation frame onto the IMU frame and using the full NAV–IMU rotation matrix, the static gyroscope measurement model can be written as

$$\boldsymbol{\omega}_{IMU} = \begin{bmatrix} \cos(\psi)\cos(\theta)\cdot\Omega_E\,\cos(\lambda) - \sin(\theta)\cdot\Omega_E\,\sin(\lambda) \\ -\sin(\psi)\cos(\phi)\cdot\Omega_E\,\cos(\lambda) + \cos(\psi)\sin(\theta)\sin(\phi)\cdot\Omega_E\,\cos(\lambda) + \cos(\theta)\sin(\phi)\cdot\Omega_E\,\sin(\lambda) \\ \sin(\psi)\sin(\phi)\cdot\Omega_E\,\cos(\lambda) + \cos(\psi)\sin(\theta)\cos(\phi)\cdot\Omega_E\,\cos(\lambda) + \cos(\theta)\cos(\phi)\cdot\Omega_E\,\sin(\lambda) \end{bmatrix} + \\ + \begin{bmatrix} b_X^{\omega} \\ b_Y^{\omega} \\ b_Z^{\omega} \end{bmatrix} \tag{6.21}$$

By taking into account the linearized rotation matrix from NAV frame to IMU one, that is

$$R_{NAV}^{IMU} \approx \begin{bmatrix} 1 & \psi & -\theta \\ -\psi & 1 & \phi \\ \theta & -\phi & 1 \end{bmatrix} \tag{6.22}$$

the Earth rotation vector expressed in the IMU frame, $\boldsymbol{\Omega}_{E_{IMU}}$, is

$$\boldsymbol{\Omega}_{E_{IMU}} = R_{NAV}^{IMU} \cdot \boldsymbol{\Omega}_{E_{NAV}} \approx \begin{bmatrix} \Omega_E\,\cos(\lambda) - \theta\cdot\Omega_E\,\sin(\lambda) \\ -\psi\cdot\Omega_E\,\cos(\lambda) + \phi\cdot\Omega_E\,\sin(\lambda) \\ \theta\cdot\Omega_E\,\cos(\lambda) + \Omega_E\,\sin(\lambda) \end{bmatrix} \tag{6.23}$$

Hence, the gyro outputs are a sum of the contributions due to the bias errors and the projections of the Earth rotation rate on the IMU channels.

$$\boldsymbol{\omega}_{IMU} = \boldsymbol{\Omega}_{E_{IMU}} + \mathbf{b}^{\omega}$$

that is

$$\boldsymbol{\omega}_{IMU} = \begin{bmatrix} \omega_X^{IMU} \\ \omega_Y^{IMU} \\ \omega_Z^{IMU} \end{bmatrix} \approx \begin{bmatrix} \Omega_E \cos(\lambda) - \theta \cdot \Omega_E \sin(\lambda) \\ -\psi \cdot \Omega_E \cos(\lambda) + \phi \cdot \Omega_E \sin(\lambda) \\ \theta \cdot \Omega_E \cos(\lambda) + \Omega_E \sin(\lambda) \end{bmatrix} + \begin{bmatrix} b_X^\omega \\ b_Y^\omega \\ b_Z^\omega \end{bmatrix} \tag{6.24}$$

Since the pitch θ and roll ϕ angles are known from the procedure described in Section 6.2, part of the Earth rate contribution can be removed from the gyroscope measurements, that means b_X^ω and b_Z^ω can be estimated.
However, the Y-channel equation contains both the yaw angle ψ and the gyroscope bias component b_Y^ω, so this last value cannot be evaluated by means of the static data alone.

For this reason the complete 360° rotation described in Section 4.2 is analyzed in this section. This dataset provides the additional information required to remove the coupling between the gyroscope bias effects and the yaw-related misalignment effects of Equation 6.24.
The gyroscope outputs recorded during the complete rotation, after removing the acceleration and deceleration ramps, are shown in Figure 6.5.

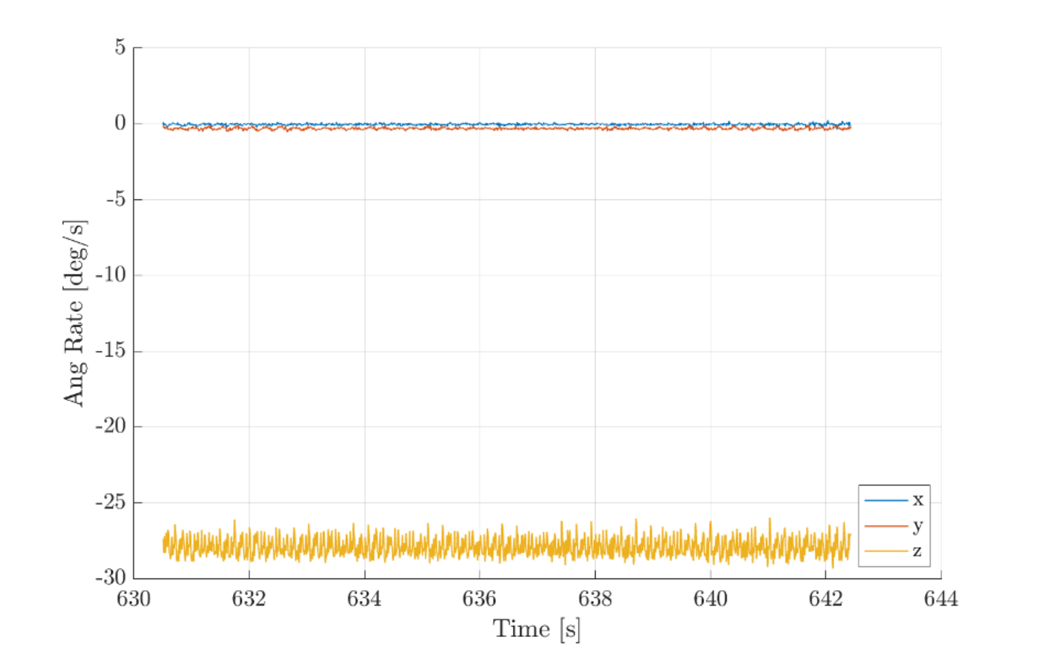

FIGURE 6.5: Gyro outputs during the 360° rotation around the $-\hat{\boldsymbol{U}}$ direction. Acceleration and deceleration ramps have been canceled out.

During the complete rotation, the gyroscope measurements contain three main contributions: the projection of the Earth rotation vector $\mathbf{\Omega}_E$ onto the IMU axes, the projection of the angular velocity imposed by the robotic arm onto the IMU axes, and the gyroscope bias vector $\mathbf{b}^{\omega}$. The angular velocity imposed by the robotic arm is expressed in the interface frame as $\boldsymbol{\omega}_{Rob_{int}} = [0,\, 0,\, \omega_{Rob}]$.

Indeed, the gyro outputs in the IMU frame can be written in the following way

$$\boldsymbol{\omega}_{IMU} = \mathbf{\Omega}_{E_{IMU}} + \boldsymbol{\omega}_{Rob_{IMU}} + \mathbf{b}^{\omega} \tag{6.25}$$

Where $\mathbf{\Omega}_E^{IMU}$ is the vector introduced in Equation 6.20 and explicitly written in Equation 6.21.

The robot angular velocity vector expressed in the IMU frame, $\boldsymbol{\omega}_{Rob}^{IMU}$, is instead obtained as

$$\boldsymbol{\omega}_{Rob_{IMU}} = R_{int}^{IMU} \cdot \boldsymbol{\omega}_{Rob_{int}} = \begin{bmatrix} -\sin(\beta) \cdot \omega_{Rob} \\ \sin(\alpha)\cos(\beta) \cdot \omega_{Rob} \\ \cos(\alpha)\cos(\beta) \cdot \omega_{Rob} \end{bmatrix} \tag{6.26}$$

Equation 6.26 shows that the interface-to-IMU misalignment angles α and β directly affect the projection of the robot angular velocity onto the IMU axes. For this reason, the values of α and β computed in Section 5.3 and shown in Table 5.2 are used here as *a priori* quantities.

The complete gyroscope measurement model during the 360° rotation can therefore be written as

$$\begin{aligned} \boldsymbol{\omega}_{IMU} = \begin{bmatrix} \omega_X^{IMU} \\ \omega_Y^{IMU} \\ \omega_Z^{IMU} \end{bmatrix} &\approx \begin{bmatrix} \Omega_E\, \cos(\lambda) - \theta \cdot \Omega_E\, \sin(\lambda) \\ -\psi(t) \cdot \Omega_E\, \cos(\lambda) + \phi \cdot \Omega_E\, \sin(\lambda) \\ \theta \cdot \Omega_E\, \cos(\lambda) + \Omega_E\, \sin(\lambda) \end{bmatrix} + \\ &+ \begin{bmatrix} -\sin(\beta) \cdot \omega_{Rob} \\ \sin(\alpha)\cos(\beta) \cdot \omega_{Rob} \\ \cos(\alpha)\cos(\beta) \cdot \omega_{Rob} \end{bmatrix} + \begin{bmatrix} b_X^{\omega} \\ b_Y^{\omega} \\ b_Z^{\omega} \end{bmatrix} \end{aligned} \tag{6.27}$$

The complete rotation model should also include the rotation around the $\hat{\boldsymbol{Z}}_{int}$ axis introduced by the PA10 robotic arm during the complete 360° motion. This contribution can be represented by the rotation matrix

$$R = \begin{bmatrix} \cos(\omega_{Rob}\, t) & \sin(\omega_{Rob}\, t) & 0 \\ -\sin(\omega_{Rob}\, t) & \cos(\omega_{Rob}\, t) & 0 \\ 0 & 0 & 1 \end{bmatrix} \tag{6.28}$$

This matrix describes the time-dependent rotation of the PA10 around the vertical axis of the interface frame. Therefore, a complete derivation would require including this additional rotation in the full attitude model. The complete mathematical development, including the rotation of the platform and the simplifications leading to the equations used in this thesis, is reported in the internal methodology developed in [17].
In the present analysis, the explicit contribution of Equation 6.28 is not carried through the following equations, because its symmetric effect over the complete rotation is canceled by the integration used to estimate the gyroscope biases. For this reason, only the time variation of the yaw angle, $\psi = \psi(t)$, is reported explicitly.

The angles α and β are known from the laboratory characterization described in Section 5.3, while θ and ϕ are known from the static attitude estimation described in Section 6.2. Their numerical values are reported in Tables 5.2 and 7.7, respectively.
Therefore, all the contributions associated with these known angles can be subtracted from the raw gyroscope data, and the simplified equations read as follows.

$$\begin{cases} \omega_X^{IMU} - \Omega_E \cos(\lambda) + \theta \cdot \Omega_E \sin(\lambda) + \sin(\beta) \cdot \omega_{Rob} = b_X^{\omega} & \rightarrow \omega_X^{NoMis} \\ \omega_Y^{IMU} - \phi \cdot \Omega_E \sin(\lambda) - \sin(\alpha)\cos(\beta) \cdot \omega_{Rob} = b_Y^{\omega} - \psi(t) \cdot \Omega_E \cos(\lambda) & \rightarrow \omega_Y^{NoMis} \\ \omega_Z^{IMU} - \theta \cdot \Omega_E \cos(\lambda) - \cos(\alpha)\cos(\beta) \cdot \omega_{Rob} = b_z^{\omega} & \rightarrow \omega_Z^{NoMis} \end{cases} \tag{6.29}$$

As mentioned above, the imposed rotation introduces a time variation of the yaw angle, so that $\psi = \psi(t)$. During the complete rotation, the yaw angle follows an oscillatory behavior around its initial value ψ_0. When the platform returns to its initial orientation, the IMU also returns to the same yaw configuration, closing the oscillatory motion. This property allows the yaw dependent contribution to be canceled by integrating over the complete rotation interval.

Without applying the small angle linearization to the yaw dependent term, the Y-channel output ω_Y^{NoMis}, after the removal of the known contributions, can be written as

$$-\Omega_E \cos(\lambda) \cdot \sin(\omega_{Rob}\, t + \psi_0) + b_Y^\omega \tag{6.30}$$

The sinusoidal term in Equation 6.30 is induced by the rotation imposed by the PA10 and is characterized by:

- **Amplitude:** $\Omega_E \cos(\lambda)$, that is the component of the Earth angular velocity projected onto the horizontal plane $[\hat{\boldsymbol{N}}, \hat{\boldsymbol{W}}]$ of the navigation frame;
- **Period:** $T = {}^{2\pi}/_{\omega_{Rob}}$;
- **Initial Phase:** ψ_0, that is the initial yaw misalignment between the navigation frame and the IMU frame.

The sinusoid oscillates around the constant value of the Y-channel gyroscope bias b_Y^ω.
A similar oscillatory behavior can also be observed in the X-channel output. This effect is induced by the time variation of the yaw angle during the imposed rotation, although it is not explicitly visible in the linearized equations reported above because of the small angle approximation.
As for the robot rotation terms, the symmetric fluctuating contributions are canceled by the integration over the complete rotation interval.

Therefore, by integrating ω_Y^{NoMis} over one complete rotation period, the Y-channel gyroscope bias can be extracted as

$$b_Y^\omega = \frac{1}{T} \int_0^T \omega_Y^{NoMis}(t)\, dt \tag{6.31}$$

Consequently, the yaw angle is computed using the expression of the static Y-channel gyroscope output introduced in Equation 6.24. In this computation, the mean static gyroscope output acquired with the IMU kept still and with the $\hat{\boldsymbol{Z}}_{IMU}$ axis approximately aligned with $\hat{\boldsymbol{U}}$ is considered.
Therefore, the yaw angle is obtained as

$$\psi = \frac{\omega_Y^{static} - \phi \cdot \Omega_E \sin(\lambda) - b_Y^{\omega}}{-\Omega_E \cos(\lambda)} \tag{6.32}$$

The yaw value obtained through Equation 6.32 is compared with the corresponding reference NAV–IMU misalignment angle reported in Table 7.4. The comparison is shown in Table 7.7

To improve the accuracy of the final gyroscope bias evaluation, the static gyroscope data are then used together with the estimated attitude angles. This makes it possible to avoid the small-angle linearization and to compute the gyroscope biases from the complete expression obtained by multiplying the full R_{NAV}^{IMU} matrix by the Earth rotation vector $\boldsymbol{\Omega}_E$.
The resulting equations are

$$b_X^{\omega} = \omega_X^{static} - \cos(\psi)\cos(\theta) \cdot \Omega_E \cos(\lambda) + \sin(\theta) \cdot \Omega_E \sin(\lambda) \tag{6.33a}$$

$$\begin{aligned} b_Y^{\omega} = \omega_Y^{static} &+ \sin(\psi)\cos(\phi) \cdot \Omega_E \cos(\lambda) + \\ &- \cos(\psi)\sin(\theta)\sin(\phi) \cdot \Omega_E \cos(\lambda) - \cos(\theta)\sin(\phi) \cdot \Omega_E \sin(\lambda) \end{aligned} \tag{6.33b}$$

$$\begin{aligned} b_Z^{\omega} = \omega_Z^{static} &- \sin(\psi)\sin(\phi) \cdot \Omega_E \cos(\lambda) + \\ &- \cos(\psi)\sin(\theta)\cos(\phi) \cdot \Omega_E \cos(\lambda) - \cos(\theta)\cos(\phi) \cdot \Omega_E \sin(\lambda) \end{aligned} \tag{6.33c}$$

Therefore, the procedure provides the estimated gyroscope biases and the yaw angle, completing the set of calibration and alignment parameters evaluated in the real-case scenario.

The final gyroscope biases computed through Equations 6.33 are reported in Chapter 7, Table 7.8, where they are compared with the corresponding bench true values.

CHAPTER 7

Results

First, the constants and experimental settings used in the calibration and alignment procedure are reported. These values are used throughout the data processing described in Chapter 6.

Parameter	Value
Local Gravity (Très Cantos) g_0	9.79956 $^m/_{s^2}$
Earth rotation rate Ω_E	15.0411 $^\circ/_h$
Latitude (Très Cantos) λ	40.59129 °
IMU sampling frequency f_{sampl}	125 Hz

Table 7.1: Constants and experimental settings used in the auto-calibration and auto-alignment procedure.

The angular velocity imposed by the robotic arm, $\boldsymbol{\omega}_{Rob}$, is extracted from the robot telemetry. The telemetry data used for the complete 360° rotation are shown in Figure 7.1. The acceleration and deceleration ramps have been removed, so that only the constant-speed portion of the motion is considered.

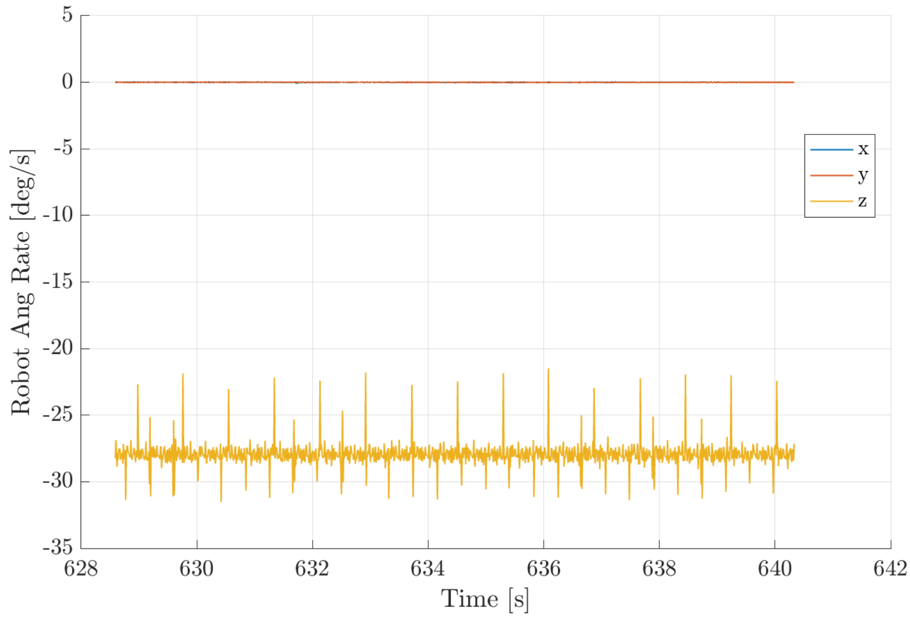

FIGURE 7.1: Angular rate saved by the robot telemetry during the full rotation. The acceleration and deceleration ramps have been removed.

The mean gyroscope outputs measured during the same complete rotation are reported in Table 7.2. The norm of these values is then compared with the angular velocity obtained from the robot telemetry in Table 7.3. The close agreement between the angular rate magnitude reconstructed from the gyroscope outputs and the angular velocity extracted from the robot telemetry confirms the consistency between the IMU measurements and the robotic motion.

At the same time, the distribution of the measured angular rate among the three gyroscope channels, reported in Table 7.2 and illustrated in Figure 5.4, shows that the imposed rotation is not measured only along a single IMU axis. This behavior is consistent with the presence of a small interface-to-IMU misalignment, which affects the projection of the robot angular velocity onto the IMU axes, as discussed in Section 5.3.

Gyro X-channel ω_X [$^\circ/_s$]	**Gyro Y-channel ω_Y [$^\circ/_s$]**	**Gyro Z-channel ω_Z [$^\circ/_s$]**
-0.0583	-0.2891	-27.9187

TABLE 7.2: Mean gyroscope outputs measured during the constant-speed portion of the complete 360° rotation.

$\boldsymbol{\omega}$ **from Robot telemetry** $|\boldsymbol{\omega}_{Rob}|$ $[^{\circ}/_{s}]$	$\boldsymbol{\omega}$ **from Gyro Outputs** $|\boldsymbol{\omega}_{Gyro}|$ $[^{\circ}/_{s}]$
27.9295	27.9204

Table 7.3: Comparison between the angular velocity magnitude extracted from the robot telemetry and the one reconstructed from the gyroscope outputs.

The bench true bias values computed with the laboratory calibration procedure described in Chapter 5 are reported in Table 5.1. These values are used as reference quantities for the validation of the real-case calibration procedure.

Before presenting the results of the real-case calibration and alignment procedure, reference values for the NAV–IMU misalignment angles are introduced. These values are used as bench true parameters for the validation of the estimated pitch θ, roll ϕ, and yaw ψ angles.
The reference angles are obtained by applying the same estimation procedure described in Section 6.2, but subtracting the bench true inclinometer biases computed in Chapter 5 (see Table 5.1), instead of the biases estimated in Section 6.1. In this way, the comparison is performed with respect to attitude parameters derived from the same mathematical framework, while relying on laboratory calibrated bias values as reference quantities.

The resulting reference NAV–IMU misalignment angles are reported in Table 7.4.

Pitch $\boldsymbol{\theta}$ $[^{\circ}]$	**Roll** $\boldsymbol{\phi}$ $[^{\circ}]$	**Yaw** $\boldsymbol{\psi}$ $[^{\circ}]$
-0.3205	0.8193	-3.0360

Table 7.4: Reference NAV–IMU misalignment angles used for the validation of the real-case alignment procedure. These values are obtained by applying the same estimation procedure described in Chapter 6, but using the bench true bias values computed in laboratory conditions.

The inclinometer biases estimated with the procedure described in Section 6.1 are reported in Table 7.5, together with the corresponding bench true values. The Z-channel inclinometer bias is assumed to be zero in the real-case procedure, as explained in Section 6.1.

INC Bias	**X-channel**	**Y-channel**	**Z-channel**
Bench true [mg]	-0.8990	-0.6567	-0.2351
Computed [mg]	-0.5778	-0.5206	0
Absolute Error [mg]	0.3212	0.1361	0.2351
Relative Error [-]	0.5558	0.2614	-

TABLE 7.5: Comparison between bench true and estimated inclinometer biases in the nominal real-case procedure.

After estimating the inclinometer biases, the corrected inclinometer outputs are used to evaluate the pitch θ and roll ϕ angles, as described in Section 6.2. These angles are then used to compute the accelerometer biases from the static accelerometer measurements.
The results obtained for the accelerometer biases are reported in Table 7.6.

ACC Bias	**X-channel**	**Y-channel**	**Z-channel**
Bench true [mg]	-1.2811	7.0304	0.5056
Computed [mg]	-0.9975	7.1957	0.5636
Absolute Error [mg]	0.2836	0.1653	0.0581
Relative Error [-]	0.2843	0.0230	0.1030

TABLE 7.6: Comparison between bench true and estimated accelerometer biases in the nominal real-case procedure.

The complete NAV–IMU misalignment can then be evaluated by combining the pitch and roll estimation described in Section 6.2 with the yaw estimation described in Section 6.3.
The estimated angles are compared with the reference values introduced in Table 7.4. The comparison is reported in Table 7.7.

NAV–IMU angles	**Pitch θ**	**Roll ϕ**	**Yaw ψ**
Reference [°]	-0.3205	0.8193	-3.0360
Computed [°]	-0.3019	0.8117	24.9105
Absolute Error [°]	0.0186	0.0076	27.9465
Relative Error [-]	0.0616	0.0094	1.1219

Table 7.7: Comparison between reference and estimated NAV–IMU misalignment angles in the nominal real-case procedure.

The gyroscope biases computed through the procedure described in Section 6.3 are reported in Table 7.8. The comparison with the bench true values shows that the X and Z gyroscope bias components are estimated with good accuracy, while the Y-channel bias is more affected by the error in the yaw estimation.

Gyro Bias	**X-channel**	**Y-channel**	**Z-channel**
Bench true [$^{\circ}/_{h}$]	98.6017	-34.7380	-27.4377
Computed [$^{\circ}/_{h}$]	97.5610	-29.3344	-28.2015
Absolute Error [$^{\circ}/_{h}$]	1.0408	5.4036	0.7638
Relative Error [-]	0.0107	0.1842	0.0271

Table 7.8: Comparison between bench true and estimated gyroscope biases in the nominal real-case procedure.

It can be observed from Table 7.7 that the error on the yaw angle ψ is significantly larger than the errors obtained for pitch and roll. This behavior is mainly related to the sensitivity of the gyroscope-based estimation to the interface-to-IMU misalignment angles α and β.

In the nominal real-case procedure, these angles are treated as *a priori* parameters and are taken from the laboratory mean values reported in Table 5.2. Since these values are obtained from rotation datasets different from the dataset used in the real-case gyroscope analysis, residual errors may remain

when the robot angular rate contribution is removed from the gyroscope outputs.
For this reason, two additional analyses are reported in the following sections. The first one evaluates the effect of using dataset-specific nonlinear values of α and β, while the second one investigates a linear same-dataset method for estimating these angles without relying on bench true gyroscope biases.

7.1 Sensitivity Analysis on the Interface-to-IMU Misalignment Angles

As discussed in the previous section, the largest error obtained in the nominal real-case procedure is associated with the yaw angle ψ and with the Y-channel gyroscope bias b^{ω}_{Y}. This behavior is mainly related to the sensitivity of the gyroscope-based estimation to the interface-to-IMU misalignment angles α and β.
In the nominal real-case procedure described in Chapter 6, the angles α and β are treated as *a priori* parameters. In particular, the values used in the nominal analysis are the laboratory values reported in Table 5.2. These values are obtained from rotation datasets different from the dataset used in the real-case calibration and alignment procedure.
This choice is consistent with the objective of the nominal procedure, since α and β are assumed to be known before applying the real-case calibration method. However, the results reported in Chapter 7 show that even very small errors in these angles can strongly affect the yaw estimation.

For this reason, the first analysis presented in this chapter is not intended as a new nominal procedure, but as a sensitivity check. The objective is to verify whether the large yaw error observed in Table 7.7 is mainly caused by the accuracy of the *a priori* values of α and β.
To perform this check, the same real-case procedure is repeated by using interface-to-IMU misalignment angles computed from the same rotation dataset used in Section 6.3. These values are obtained through the non-linear procedure described in Section 5.3 and are reported in Table 5.3. Since this computation relies on information that would not be available in a fully autonomous operational scenario, these values are not used in the nominal procedure. Nevertheless, they are useful to understand the sensitivity of the method to the accuracy of α and β.

The comparison between the nominal laboratory values and the same-dataset values of α and β is reported in Table 7.9.

Source	$\boldsymbol{\alpha}$ [°]	$\boldsymbol{\beta}$ [°]
Nominal laboratory values	0.5964	-0.1125
Nonlinear same-dataset method	0.5934	-0.1196
Absolute Difference [°]	0.0030	0.0071

TABLE 7.9: Comparison between the nominal laboratory interface-to-IMU misalignment angles evaluated from different datasets and the same-dataset nonlinear values used for the sensitivity analysis.

The real-case procedure is then repeated using the same-dataset nonlinear values of α and β. The corresponding inclinometer bias results are reported in Table 7.10.

INC Bias	**X-channel**	**Y-channel**	**Z-channel**
Bench true [mg]	-0.8990	-0.6567	-0.2351
Computed [mg]	-0.7009	-0.4689	0
Absolute Error [mg]	0.1981	0.1878	0.2351
Relative Error [-]	0.2826	0.4005	-

TABLE 7.10: Comparison between bench true and estimated inclinometer biases obtained using the same-dataset nonlinear values of α and β.

The accelerometer bias results obtained with the same values of α and β are reported in Table 7.11.

ACC Bias	**X-channel**	**Y-channel**	**Z-channel**
Bench true [mg]	-1.2811	7.0304	0.5056
Computed [mg]	-1.1205	7.2474	0.5636
Absolute Error [mg]	0.1605	0.2170	0.0580
Relative Error [-]	0.1433	0.0299	0.1029

Table 7.11: Comparison between bench true and estimated accelerometer biases obtained using the same-dataset nonlinear values of α and β.

The resulting NAV–IMU misalignment angles are reported in Table 7.12. Compared with the nominal results shown in Table 7.7, the yaw estimation improves significantly when the same-dataset values of α and β are used.

NAV–IMU angles	**Pitch θ**	**Roll ϕ**	**Yaw ψ**
Reference [°]	-0.3205	0.8193	-3.0360
Computed [°]	-0.3090	0.8087	-1.2668
Absolute Error [°]	0.0115	0.0106	1.7692
Relative Error [-]	0.0374	0.0131	1.3966

Table 7.12: Comparison between reference and estimated NAV–IMU misalignment angles obtained using the same-dataset nonlinear values of α and β.

The corresponding gyroscope bias results are reported in Table 7.13. The improvement is particularly evident for the Y-channel gyroscope bias.

Gyro Bias	X-channel	Y-channel	Z-channel
Bench true [$°/_h$]	98.6017	-34.7380	-27.4377
Computed [$°/_h$]	96.5029	-34.3828	-28.1230
Absolute Error [$°/_h$]	2.0989	0.3552	0.6853
Relative Error [-]	0.0217	0.0103	0.0244

TABLE 7.13: Comparison between bench true and estimated gyroscope biases obtained using the same-dataset nonlinear values of α and β.

The results reported in Tables 7.10–7.13 confirm that the accuracy of the interface-to-IMU misalignment angles has a strong impact on the final yaw and gyroscope bias estimation. In particular, the yaw error decreases significantly with respect to the nominal case reported in Chapter 7. This confirms that the large yaw error obtained in the nominal procedure is not mainly caused by the mathematical formulation itself, but by the sensitivity of the method to the *a priori* values of α and β.

In addition, the results show an improvement in the inclinometer biases and, consequently, in the accelerometer biases.
This behavior is consistent with the propagation of the errors on α and β. In particular, the differences of 0.0030° on α and 0.0071° on β produce an error of approximately 0.1239 mg in the X-channel inclinometer bias and 5.26 $°/_h$ in the Y-channel gyroscope bias. These values are consistent with the improvements observed in the second run of the code.

7.2 Linear same-dataset estimation of the interface-to-IMU Misalignment

The same-dataset nonlinear analysis cannot be considered as a fully operational solution. The reason is that it relies on information that is not available in the real-case autonomous procedure. In particular, the nonlinear same-dataset estimation uses the rotational gyroscope outputs after removing the bench true gyroscope biases. Therefore, it is useful as a sensitivity analysis, but it cannot be used as the nominal method when the IMU is already mounted on the final platform and no laboratory bench true values are available.

This observation motivates the development of a different strategy. The objective is to estimate α and β from the same mounted IMU dataset used in the real-case procedure, but without relying on the bench true gyroscope biases. A possible solution is to exploit a linear procedure based on the subtraction between dynamic gyroscope data and static gyroscope data.

The idea is to subtract the static gyroscope outputs from the gyroscope outputs recorded during the complete rotation. By doing this, the constant gyroscope bias contribution and the static Earth rate contribution can be removed. The remaining term is mainly associated with the projection of the robot angular velocity $\boldsymbol{\omega}_{Rob}$ onto the IMU axes.

In formulas, the exact gyroscope output during the complete 360° rotation can be written without applying the linearization assumption as

$$\boldsymbol{\omega}_{IMU}^{Rot} = \begin{bmatrix} \cos(\psi)\cos(\theta)\cdot\Omega_E\,\cos(\lambda) - \sin(\theta)\cdot\Omega_E\,\sin(\lambda) \\ -\sin(\psi)\cos(\phi)\cdot\Omega_E\,\cos(\lambda) + \cos(\psi)\sin(\theta)\sin(\phi)\cdot\Omega_E\,\cos(\lambda) + \cos(\theta)\sin(\phi)\cdot\Omega_E\,\sin(\lambda) \\ \sin(\psi)\sin(\phi)\cdot\Omega_E\,\cos(\lambda) + \cos(\psi)\sin(\theta)\cos(\phi)\cdot\Omega_E\,\cos(\lambda) + \cos(\theta)\cos(\phi)\cdot\Omega_E\,\sin(\lambda) \end{bmatrix} + \\ + \begin{bmatrix} -\sin(\beta)\cdot\omega_{Rob} \\ \sin(\alpha)\cos(\beta)\cdot\omega_{Rob} \\ \cos(\alpha)\cos(\beta)\cdot\omega_{Rob} \end{bmatrix} + \begin{bmatrix} b_X^\omega \\ b_Y^\omega \\ b_Z^\omega \end{bmatrix} \tag{7.1}$$

And the corresponding static gyroscope output can be written as

$$\boldsymbol{\omega}_{IMU}^{Stat} = \begin{bmatrix} \cos(\psi)\cos(\theta)\cdot\Omega_E\,\cos(\lambda) - \sin(\theta)\cdot\Omega_E\,\sin(\lambda) \\ -\sin(\psi)\cos(\phi)\cdot\Omega_E\,\cos(\lambda) + \cos(\psi)\sin(\theta)\sin(\phi)\cdot\Omega_E\,\cos(\lambda) + \cos(\theta)\sin(\phi)\cdot\Omega_E\,\sin(\lambda) \\ \sin(\psi)\sin(\phi)\cdot\Omega_E\,\cos(\lambda) + \cos(\psi)\sin(\theta)\cos(\phi)\cdot\Omega_E\,\cos(\lambda) + \cos(\theta)\cos(\phi)\cdot\Omega_E\,\sin(\lambda) \end{bmatrix} + \\ + \begin{bmatrix} b_X^{\omega} \\ b_Y^{\omega} \\ b_Z^{\omega} \end{bmatrix} \tag{7.2}$$

Therefore, by subtracting Equation 7.2 from Equation 7.1, both the gyroscope bias vector and the static Earth rate contribution are removed.
The resulting expression is

$$\boldsymbol{\omega}_{IMU}^{Rot} - \boldsymbol{\omega}_{IMU}^{Stat} = \begin{bmatrix} -\sin(\beta)\cdot\omega_{Rob} \\ \sin(\alpha)\cos(\beta)\cdot\omega_{Rob} \\ \cos(\alpha)\cos(\beta)\cdot\omega_{Rob} \end{bmatrix} \tag{7.3}$$

From Equation 7.3, the angles α and β can be estimated.

This method has been implemented to verify whether it can improve the estimation with respect to the nominal laboratory values of α and β reported in Table 5.2.
The comparison between the nominal laboratory values and the values obtained with the linear same-dataset method is reported in Table 7.14.

Method	$\boldsymbol{\alpha}$ [°]	$\boldsymbol{\beta}$ [°]
Nominal laboratory values	0.5964	-0.1125
Linear same-dataset method	0.5935	-0.1183
Absolute Difference [°]	0.0029	0.0058

TABLE 7.14: Comparison between the nominal laboratory interface-to-IMU misalignment angles evaluated from different datasets and the values obtained with the proposed linear same-dataset method.

The real-case procedure is then repeated using the linear same-dataset values of α and β. The inclinometer bias results are reported in Table 7.15.

INC Bias	**X-channel**	**Y-channel**	**Z-channel**
Bench true [mg]	-0.8990	-0.6567	-0.2351
Computed [mg]	-0.6782	-0.4707	0
Absolute Error [mg]	0.2208	0.1861	0.2351
Relative Error [-]	0.3255	0.3953	-

TABLE 7.15: Comparison between bench true and estimated inclinometer biases obtained using the linear same-dataset estimation of α and β.

The corresponding accelerometer bias results are reported in Table 7.16.

ACC Bias	**X-channel**	**Y-channel**	**Z-channel**
Bench true [mg]	-1.2811	7.0304	0.5056
Computed [mg]	-1.0978	7.2457	0.5635
Absolute Error [mg]	0.1832	0.2153	0.0579
Relative Error [-]	0.1669	0.0297	0.1027

TABLE 7.16: Comparison between bench true and estimated accelerometer biases obtained using the linear same-dataset estimation of α and β.

The NAV–IMU misalignment angles obtained with the linear same-dataset method are reported in Table 7.17.

NAV–IMU angles	**Pitch θ**	**Roll ϕ**	**Yaw ψ**
Reference [°]	-0.3205	0.8193	-3.0360
Computed [°]	-0.3077	0.8088	-0.3833
Absolute Error [°]	0.0128	0.0105	2.6527
Relative Error [-]	0.0417	0.0129	6.9214

Table 7.17: Comparison between reference and estimated NAV–IMU misalignment angles obtained using the linear same-dataset estimation of α and β.

Finally, the gyroscope bias results are reported in Table 7.18.

Gyro Bias	**X-channel**	**Y-channel**	**Z-channel**
Bench true [$^\circ/_h$]	98.6017	-34.7380	-27.4377
Computed [$^\circ/_h$]	96.5006	-34.2072	-28.1257
Absolute Error [$^\circ/_h$]	2.1012	0.5308	0.6880
Relative Error [-]	0.0218	0.0155	0.0245

Table 7.18: Comparison between bench true and estimated gyroscope biases obtained using the linear same-dataset estimation of α and β.

For the results reported in Tables 7.15–7.18, the dynamic data are taken from the clockwise rotation around the $-\hat{\boldsymbol{U}}$ direction, shown in Figure 6.5. The static data are taken from the interval in which the IMU is kept still with the $\hat{\boldsymbol{Z}}_{IMU}$ axis approximately aligned with the $\hat{\boldsymbol{U}}$ direction, as described in Section 6.2.

The results obtained with the proposed methodology confirm that estimating α and β from the same dataset used in the real-case procedure can significantly improve the yaw and Y-channel gyroscope bias estimation with respect to the nominal case.
Although the yaw error obtained with the linear method is slightly larger than the one obtained with the same-dataset nonlinear sensitivity analysis,

the linear approach has a more practical interest because it does not require the bench true gyroscope biases as input.

CHAPTER 8

Conclusion & Future Work

This thesis presented the experimental validation of an auto-calibration and auto-alignment methodology for a STIM300 IMU, using a PA10 robotic arm as a controlled motion platform. The work included the definition of the reference frames involved in the problem, the modeling of the main IMU error sources, the design of a dedicated experimental campaign, the implementation of both a laboratory calibration procedure and a real-case scenario representative of an already mounted sensor.

In the laboratory calibration phase, reference bias values and interface alignment parameters were derived and used as bench true quantities for the validation of the proposed method. In particular, the bench characterization allowed the estimation of reference values for the accelerometer, inclinometer, and gyroscope biases. In addition, the interface-to-IMU misalignment angles α and β were estimated in laboratory conditions and used as *a priori* parameters in the nominal real-case procedure.
In the real-case scenario, static intervals and controlled rotational motion were exploited to estimate accelerometer, inclinometer, and gyroscope biases, together with the Euler angles describing the misalignment between the navigation and IMU frames. The main outcome of the work is the experimental demonstration that controlled rotational motion provides additional information with respect to purely static initialization. In particular, the imposed rotation makes the yaw-related contribution time-varying, allowing bias and misalignment effects to be separated more effectively than in the static case. The results confirmed that the proposed method can estimate the main calibration and alignment parameters from real experimental data. At the same time, they highlighted that the accuracy of the yaw estimation is strongly limited by the accuracy of the interface-to-IMU characterization.
The sensitivity analysis performed in Section 7.1 represents one of the main

lessons learned from the experimental validation. The angles α and β determine how the angular velocity imposed by the robotic arm is projected onto the IMU axes. Therefore, even small errors in their estimation can introduce residual angular rate components after the robot contribution is removed from the gyroscope outputs. This effect was found to be particularly relevant for the estimation of the yaw angle ψ and of the corresponding Y-channel gyroscope bias component b_Y^{ω}.

A possible improvement is the development of a robust same-dataset estimation strategy for the interface-to-IMU misalignment angles. The linear approach investigated in Section 7.2 represents a first step in this direction, since it aims to estimate α and β without relying on bench true gyroscope biases. Further work should focus on improving the robustness of this method, testing it on additional datasets, and assessing its sensitivity to noise, angular rate variations, and residual non-idealities in the robot motion.

Another limitation of the present experimental setup is related to the motion imposed by the PA10 robotic arm. In the current analysis, the acceleration and deceleration ramps are removed from the rotational data, and only the approximately constant-speed portion of the motion is used. As a consequence, the integration and averaging steps are not performed over an ideal complete 360° constant-speed rotation, which can introduce residual errors in the estimated quantities.

A further improvement would be to control the robot angular velocity ω_{Rob} more precisely. Testing the procedure at different angular rates would make it possible to evaluate the sensitivity of the method to the imposed rotation speed and to identify the most suitable operating conditions for the calibration procedure.

Finally, future validation could be performed using a dedicated rotary platform, such as the one shown in Figure 8.1. A platform specifically designed for controlled rotations would allow smoother and more repeatable complete 360° rotations, better control of the angular velocity, and a more accurate validation of the proposed auto-calibration and auto-alignment methodology.

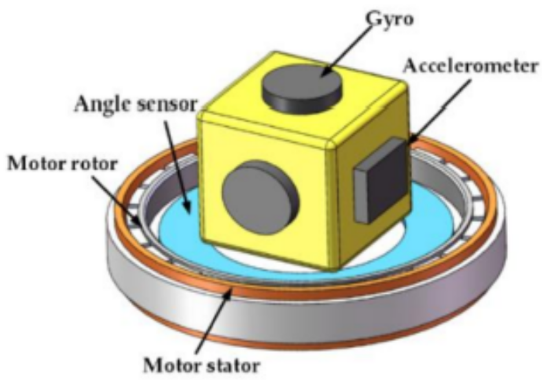

FIGURE 8.1: Example of a rotary platform (CONS) that could be used for future validation tests.

Overall, the activities carried out in this thesis achieved the objective of validating the proposed methodology on real experimental data, while also identifying the main limitations of the current implementation.
The use of controlled rotation represents a promising compromise between classical laboratory calibration and fully aided navigation approaches, since it introduces additional information through motion without requiring external measurement aiding. Future improvements should focus on increasing the accuracy of the interface-to-IMU misalignment estimation and on validating the methodology using a dedicated rotational platform and a more reliable robotic arm.

Bibliography

[1] D. Titterton and J. Weston, *Strapdown Inertial Navigation Technology*. Institution of Engineering and Technology, Jan. 2004.

[2] P. D. Groves, *Principles of GNSS, inertial, and multisensor integrated navigation systems*, second edition ed., ser. Artech House GNSS library. Boston: Artech House, 2013, includes bibliographical references and index.

[3] J. A. Farrell, *Aided navigation*, ser. Electronic engineering. New York, NY [u.a.]: McGraw-Hill, 2008, includes bibliographical references (p. 515-525) and index. - Formerly CIP.

[4] Z. F. Syed, P. Aggarwal, C. Goodall, X. Niu, and N. El-Sheimy, “A new multi-position calibration method for MEMS inertial navigation systems,” *Measurement Science and Technology*, vol. 18, no. 7, pp. 1897–1907, May 2007.

[5] D. Tedaldi, A. Pretto, and E. Menegatti, “A robust and easy to implement method for IMU calibration without external equipments,” in *2014 IEEE International Conference on Robotics and Automation (ICRA)*. IEEE, May 2014, pp. 3042–3049.

[6] H. Hou, “Modeling Inertial Sensors Errors Using Allan Variance,” Master’s thesis, University of Calgary, 2004. [Online]. Available: https://www.ucalgary.ca/engo_webdocs/NES/04.20201.HaiyingHou.pdf

[7] N. El-Sheimy, H. Hou, and X. Niu, “Analysis and Modeling of Inertial Sensors Using Allan Variance,” *IEEE Transactions on Instrumentation and Measurement*, vol. 57, no. 1, pp. 140–149, Jan. 2008.

[8] Y. Wu, H. Zhang, M. Wu, X. Hu, and D. Hu, “Observability of strapdown ins alignment: A global perspective,” *IEEE Trans. on Aerospace and*

Electronic Systems, 48(1), pp. 78-102, 2012, vol. 48, no. 1, pp. 78–102, Jan. 2011.

[9] S. Du, W. Sun, and Y. Gao, "Improving Observability of an Inertial System by Rotary Motions of an IMU," *Sensors*, vol. 17, no. 4, p. 698, Mar. 2017.

[10] H. Xing, Z. Chen, H. Yang, C. Wang, Z. Lin, and M. Guo, "Self-Alignment MEMS IMU Method Based on the Rotation Modulation Technique on a Swing Base," *Sensors*, vol. 18, no. 4, p. 1178, Apr. 2018.

[11] H. Barreno Almazán, "IMU Characterization and Study of an Auto-Calibration Procedure," Master's thesis, Universidad Carlos III de Madrid, 2024.

[12] ——, "IMU Auto-Alignment MEMO," GMV - Aerospace and Defence, Tech. Rep., 2023, internal document.

[13] *STIM300 Inertial Measurement Unit Datasheet*, Ts1524 rev.29 ed., Safran Electronics & Defense, 2023, product datasheet. [Online]. Available: https://safran-navigation-timing.com/document/stim300-datasheets/

[14] R. M. Sánchez Moreno, "IMU Robot Memo Draft v1," GMV - Aerospace and Defence, Tech. Rep., 2023, internal document.

[15] *PA10 Series Programming Manual*, Rev. 0 ed., Mitsubishi Heavy Industries, Ltd., general Purpose Robot PA10 Series.

[16] E. Di Sotto, "Navigation Sensors: Modelling and Algorithms. Notes of the Launchers and Re-entry Course," Course notes.

[17] H. Barreno Almazán, "Rotation Modulation Technique for IMU Calibration," GMV - Aerospace and Defence, Tech. Rep., 2023, internal document.

[18] T. GMV, "MOONDRONE MEMO," GMV - Aerospace and Defence, Tech. Rep., 2023, internal document.